# Northward Propagation, Initiation, and Termination of Boreal Summer Intraseasonal Oscillations in a Zonally Symmetric Model

Qiu Yang

*Center for Prototype Climate Modeling, New York University Abu Dhabi, Saadiyat Island, Abu Dhabi, UAE*

Boualem Khouider*

*Department of Mathematics and Statistics, University of Victoria, Victoria, BC, Canada*

Andrew J. Majda

*Department of Mathematics and Center for Atmosphere Ocean Science, Courant Institute of Mathematical Sciences, New York University, New York, NY, USA,*

*Center for Prototype Climate Modeling, New York University Abu Dhabi, Saadiyat Island, Abu Dhabi, UAE*

Michèle De La Chevrotière

*Meteorological Research Division, Environment and Climate Change Canada, Montreal, Quebec, Canada*

* *Corresponding author address:* Boualem Khouider, Mathematics and Statistics, University of Victoria, PO BOX 1700 STN CSC Victoria, B.C., Canada V8W 2Y2

E-mail: khouider@uvic.ca

ABSTRACT

A simple multilayer-zonally symmetric model, using a multicloud convective parameterization and coupled to a dynamical bulk atmospheric boundary layer, is used here to simulate boreal summer intra-seasonal oscillations (BSISO) in the summer monsoon trough and elucidate the underlying main physical mechanisms responsible for their initiation, propagation, and termination. Northward-moving precipitating events initiated near the equator propagate northward at roughly $1^\circ$ day$^{-1}$ and terminate near $20^\circ$ N. Unlike earlier findings, the northward propagation of precipitation anomalies, in this model, is due to the propagation of positive moisture anomalies in the northward direction, resulting from an asymmetry in the meridional velocity induced by the beta effect. From a moisture budget perspective, advection constitutes a biased intrusion of dry air into the convection center, forcing new convection events to form north of the wave disturbance, while moisture convergence supplies the precipitation sink. The BSISO events are initiated near the equator when the competing effects between first-baroclinic divergence and second-baroclinic convergence, induced by the descending branch of the Hadley cell and in situ congestus heating, respectively, become favorable to convective intensification. The termination often near $20^\circ$ N and halfway stalling of these precipitating events occur when the asymmetry in the first-baroclinic meridional winds weakens and when the negative moisture gradient to the north of the convection center becomes too strong as the anomaly exits the imposed warm pool domain.

## 1. Introduction

The intraseasonal variability of the tropical troposphere is dominated by wave-like systems with planetary scale flow patterns strongly coupled with convection and heavy rainfall known by the generic name of intra-seasonal oscillations (ISO) (Lau and Waliser 2011). The Madden-Julian Oscillation (MJO) (Madden and Julian 1971, 1972), once called the Holy grail of tropical atmospheric dynamics (Raymond 2001), has received tremendous attention since its discovery (e.g., Madden 1986; Hendon and Liebmann 1994; Hendon and Salby 1994; Hendon and Liebmann 1994; Raymond 2001; Biello and Majda 2005; Zhang 2005; Majda and Stechmann 2009; Ajayamohan et al. 2013; Jiang et al. 2015; Zhang 2013). The MJO is a planetary-scale convective envelope with an intraseasonal period of 40-60 days occurring over the Indian Ocean/Western Pacific warm pool and propagating eastward along the equator at 5 m $s^{-1}$, which typically prevails during the Northern Hemisphere winter season (Zhang 2005). As a counterpart to the MJO, the Indian monsoon boreal summer intraseasonal oscillation (BSISO) typically initiates over the equatorial Indian Ocean, propagates northward at $1^\circ$ $\text{day}^{-1}$ (about 1.29 m $s^{-1}$) and terminates around 20° North, over the Indian subcontinent during boreal summer (Lau and Waliser 2011). The early investigation of the northward propagation of tropical convection dates back to the 1970s, where Yasunari (1979, 1980) identified a northward movement of cloudiness in 30 to 40 day periods over Indian-Indian Ocean area during the summer monsoon season. It is generally believed that the life cycle of BSISO is intimately connected with the Indian monsoon and the Asian summer monsoon (Lee et al. 2013).

Since the BSISO is an important component of intraseasonal variability, the realistic simulation of BSISO should be not only a benchmark for examining skills and behaviors of present-day global climate models (GCMs), but also a potential prediction source for extending the current

2-week subseasonal-to-seasonal prediction skill (Brunet et al. 2010). With the recent developments in computing techniques and resources and satellite measurements, many efforts have been made to better simulate BSISO in cloud-resolving models (CRMs) and GCMs, in terms of its initiation, propagation and termination processes. Jiang et al. (2004), for example, looked at the spatial and temporal structures of the northward-propagating BSISO based on the analysis of both the ECHAM4 model simulation and NCEP-NCAR reanalysis. Fu and Wang (2004) conducted a series of small-perturbation experiments and they demonstrated that an atmosphere-ocean coupled model and an atmosphere-only model produce significantly different intensities of BSISO and have shown evidence of strong relationships between convection and underlying sea surface temperature (SST) variations. Seo et al. (2007) have examined the effect of air-sea coupling and the basic-state SST associated with the BSISO by using the NCEP coupled Climate Forecast System (CFS) model. To be brief, much progress in improving the BSISO simulations has been made but it is far from being satisfactory. The underlying mechanisms associated with the initiation, propagation, and termination processes of BSISO are still poorly understood. A comprehensive elucidation of these physical processes is not only a theoretical curiosity but would hopefully provide modelers and weather prediction scientists with new metrics on how to improve climate and weather forecasting models.

Many mechanisms have been proposed to explain the northward propagation of the BSISO in the past decades. Based on numerical experiments with a linear primitive equation model with a climatological basic state for the month of July obtained from reanalysis data, Wang and Xie (1997) suggested that the monsoon mean flows and spatial variation of moist static energy trap equatorial disturbances in the Northern Hemisphere (NH) summer monsoon domain while the mean Hadley circulation plays a critical role in the re-initiation of equatorial Kelvin-Rossby wave packets over the equatorial Indian Ocean. Based on both GCM simulation and NCEP-NCAR reanalysis data, Jiang et al. (2004) propose two mechanisms due to internal atmospheric dynamics for the northward propagation of the BSISO, namely, the generation of the northward displaced barotropic vorticity and the moisture-convection feedback. The first mechanism is further examined in a zonally symmetric model setup (Drbohlav and Wang 2005) and a three-dimensional intermediate model (Drbohlav and Wang 2007). By using lagged regressions of intraseasonally filtered outgoing longwave radiation (OLR), Lawrence and Webster (2002) suggested a link between the eastward and northward movement of convection, which is believed to be consistent with an interpretation of the BSISO in terms of propagating equatorial modes. Besides, Rossby waves emitted by equatorial convection and air-sea interactions are found to play a critical role in the BSISO dynamics (Kemball-Cook and Wang 2001).

Among most of the theoretical and numerical studies based on intermediate models, the warm surface temperature near the equatorial regions received much less attention as that over the Indian monsoon regions. As pointed out by Sikka and Gadgil (1980), there exists a seesaw characteristic of maximum cloud zones over the Indian longitude 70° E – 90° E, one of which is near the equator and the other of which is along 15° N, consistent with the simulations of Ajayamohan et al. (2014).

Meanwhile, in aforementioned models (Wang and Xie 1997; Drbohlav and Wang 2005, 2007), the nonlinear advection terms in momentum and thermal equations are replaced by mean flow advection by assuming that the BSISO is relatively small perturbation. Such simplified models also ignore the possible internal mechanisms involving nonlinear advection effects. Motivated by these limitations and the success of a recently developed multicloud parameterization technique, mimicking the main cloud types observed in the tropics and their interactions with the environment, in reproducing the key observational features of the tropical modes of variability associated with organized convection, including northward propagating BSISOs, in both simple models (Khouider and Majda 2006, 2008b,a; Waite and Khouider 2009) and GCMs (Khouider et al. 2011;

Ajayamohan et al. 2013, 2014; Goswami et al. 2017a), a 3.5-layer intermediate model, including the barotropic, first- and second-baroclinic modes in the free troposphere and a bulk atmospheric boundary layer (ABL) is used to simulate BSISO events and illustrate possible underlying mechanisms to explain its behavior as observed in nature. The model, first developed and validated in De La Chevrotière and Khouider (2017), is zonally symmetric, as in Drbohlav and Wang (2007), to focus on the northward propagating disturbances. To mimic the northward migration of the intertropical convergence zone (ITCZ) during the summer monsoon (Ajayamohan et al. 2014), a background SST resembling the mean summer (JJA), observed Indian Ocean SST climatology is imposed by means of the latent heat flux at the surface of the computational domain.

The new model successfully simulates both the climatological mean monsoon circulation and northward-moving intraseasonal anomalies. Consistent with observations, the climatological mean meridional-vertical circulation is characterized by a Hadley-like cell extending over the middle and upper troposphere with strong upward motion at low latitudes of the NH and weak downward motion in the Southern Hemisphere (SH). The northward-moving precipitating events are initiated near the equator, between 5° S and 5° N, propagate northward at the speed or roughly 1 ° day $^{-1}$ and eventually terminate near 20° N. Their vertical structure is characterized by an overturning circulation in the middle and upper troposphere. Unlike earlier findings by Wang and collaborators (e.g. Drbohlav and Wang 2005), the northward propagation of precipitation anomalies, here, is due to the propagation of positive moisture anomalies in the northward direction, resulting from an asymmetry in the meridional velocity induced by the beta effect. From a moisture budget perspective, the advection term constitutes an intrusion of dry air into the convection center while moisture convergence supplies the precipitation sink. The asymmetry in meridional advection means more dry air is introduced to the southern side of the convection center and shuts convection there forcing the whole system to move northward. The northward propagating BSISO anomalies are initiated near the equator where competing effects between first-baroclinic divergence and second-baroclinic convergence, induced by the descending branch of the Hadley cell and in situ congestus heating, respectively, take place in the lower troposphere. As the northward-moving precipitating events diminish at higher latitudes, the downward branch of this Hadley-type circulation near the equator also diminish, resulting in the dominant second-baroclinic wind convergence near the equator thanks to the prevailing congestus-type convection. This results in significant mid-troposphere moisture convergence, due to second baroclinic mode, and the intensification of convection, which then begins to slowly move Northward and accelerates when it reaches higher latitudes where the beta effect is stronger. The termination often near $20^\circ$ N and halfway stalling of these precipitating events occur when the asymmetry in the first-baroclinic meridional winds weakens and when the negative moisture gradient to the north of the convection center becomes too strong as the anomaly approaches the imposed warm pool boundary.

The paper is organized as follows. Section 2 reviews the model equations and the multicloud parameterization as well as the data used for the imposed SST profile. Section 3 presents the numerical simulation results where both the mean climatology and the northward propagating BSISO anomalies are presented and their physical features analyzed. A detailed budget of the moisture equation is given and analyzed in Section 4, where the beta induced asymmetry is explained in the light of a simplified dry shallow water wave-model. The initiation, stalling and termination mechanisms are discussed in Section 5 while a summary discussion is given in Section 6.

## 2. Data, model, and methodology

### *a. The zonally symmetric multicloud model with boundary layer dynamics*

The multilayer dynamical core used here is derived in De La Chevrotière and Khouider (2017) based on the hydrostatic Boussinesq equations on the equatorial $\beta$-plane for the free troposphere with zonal symmetry, which are written below in dimensional units of tropical synoptic scale dynamics, where the first baroclinic gravity wave speed of $c \approx 50$ m s$^{-1}$ is the reference scale for horizontal velocity components, the equatorial Rossby deformation radius of $L_e = \sqrt{c/\beta} \approx 1500$ km is the horizontal length scale, and the eddy turn over time $T_e = \sqrt{c\beta} \approx 8.33$ hours is the time scale, with $\beta$ the gradient of the Coriolis parameter at the equator. The temperature fluctuations scale is set to $\sim 15$ K so that both $\beta$ and the background potential temperature stratification $\frac{d\bar{\theta}}{dz}$ are unity in those new dimensional units. The height of the troposphere $H_T = 16$ km is used as a reference vertical coordinate scale and $W = H_T/T_e \approx 53$ cm s$^{-1}$ is used as a vertical velocity scale. We have

$$\frac{\partial u}{\partial t} + v\frac{\partial u}{\partial y} + w\frac{\partial u}{\partial z} - yv = \mathcal{S}^u, \tag{1a}$$
$$\frac{\partial v}{\partial t} + v\frac{\partial v}{\partial y} + w\frac{\partial v}{\partial z} + yu = -\frac{\partial p}{\partial y} + \mathcal{S}^v, \tag{1b}$$
$$\frac{\partial \theta}{\partial t} + v\frac{\partial \theta}{\partial y} + w\frac{\partial \theta}{\partial z} + w = \mathcal{H}^\theta + \mathcal{S}^\theta, \tag{1c}$$
$$\frac{\partial p}{\partial z} = \theta, \tag{1d}$$
$$\frac{\partial v}{\partial y} + \frac{\partial w}{\partial z} = 0, \tag{1e}$$

where $\mathcal{S}^u, \mathcal{S}^v$ represent momentum turbulent drag, and $\mathcal{H}^\theta, \mathcal{S}^\theta$ stand for diabatic heating and radiative cooling, respectively.

Eqs.1a-1e are projected onto the barotropic, first and second baroclinic modes following the Galerkin expansion:

$$\begin{pmatrix} \boldsymbol{u} \\ p \end{pmatrix}(y,z,t) = \begin{pmatrix} \boldsymbol{u}_0 \\ p_0 \end{pmatrix}(y,t) + \begin{pmatrix} \boldsymbol{u}_1 \\ p_1 \end{pmatrix}(y,t)\,C_1(z) + \begin{pmatrix} \boldsymbol{u}_2 \\ p_2 \end{pmatrix}(y,t)\,C_2(z) \quad (2)$$

$$\begin{pmatrix} \theta \\ w \end{pmatrix}(y,z,t) = \begin{pmatrix} 0 \\ w_0 \end{pmatrix}(y,t) + \begin{pmatrix} \theta_1 \\ w_1 \end{pmatrix}(y,t)\,S_1(z) + \begin{pmatrix} 2\theta_2 \\ w_2 \end{pmatrix}(y,t)\,S_2(z) \quad (3)$$

where $C_j(z) = \sqrt{2}\cos(jz)$ and $S_j(z) = \sqrt{2}\sin(jz)$ corresponds to the barotropic ($j = 0$), the first baroclinic ($j = 1$) and second baroclinic ($j = 2$) modes, respectively. The three fully coupled shallow-water like systems are strongly coupled with each other through nonlinear advection terms.

The equations in (1e.a)-(1e.e) are supplemented with the multicloud parameterization diagnostic and prognostic equations, bulk ABL dynamics and moist thermodynamics equations, obtained by averaging the primitive equations over the thin ABL constant height, and an equation for the vertically averaged moisture (Waite and Khouider 2009). To close the bulk ABL dynamic equations, continuity of pressure and vertical velocity, at the ABL top interface, is assumed. This in particular provides dynamical coupling between the ABL dynamics and the free tropospheric barotropic flow (Waite and Khouider 2009; De La Chevrotière and Khouider 2017).

For the sake of streamlining, the dynamical model equations are listed in Table 1, where the barotropic and first and second baroclinic variables are indexed by 0,1,2, respectively, while the ABL variables are indexed by the letter $b$. Notice the presence of cross indexed terms in the free tropospheric equations. In addition to continuity of pressure and vertical velocity, the ABL and free tropospheric dynamics are coupled through the entrainment and detrainment turbulent mixing terms due to shallow cumulus activity and downdraft, which appear on the right of the ABL equations in Table 1, involving variables such as $E, E_u, \Delta_t u$ and $M_d$. As can be seen from

Table 2, similar terms appear as momentum damping in the free troposphere (closure equations of $S_u$ and $S_v$) and as source of mid-tropospheric moisture. Table 2 lists all the closure equations of the multicloud model with ABL dynamics (Waite and Khouider 2009). Worthy noting, the diabatic heating terms on the right of the $\theta_1$ and $\theta_2$ equations involve convective heating due to congestus, deep, and stratiform heating ($H_c, H_d$ and $H_s$, respectively) corresponding to the main three cloud types that characterize organized tropical convective systems (Johnson et al. 1999; Khouider and Majda 2006) and radiative cooling terms consisting of background climatological values $Q_{R,j}, j = 1,2$ and Newtonian cooling terms.

The values of the parameters and model constants are listed in Table 3. More details on this multicloud model with ABL dynamics are found in Waite and Khouider (2009) and De La Chevrotière and Khouider (2017).

To handle this highly nonlinear, non conservative, and non hyperbolic system, without adding artificial viscosity, the equations in Table 1 are solved numerically using an operator splitting method where the dynamical equations are divided into a conserved system, a hyperbolic system, and a nilpotent system of equations, which are then discretized with appropriate methods. The details are found in De La Chevrotière and Khouider (2017) where the numerical method was developed and validated; the same technique has been used in Khouider and Majda (2005) and Stechmann et al. (2008) for similar nonlinear multi-mode systems. The equations are solved on a meridional domain extending from 40° South to 40° North using no flow boundary conditions. We used a spatial resolution $\Delta y = 36$ km and a time step $\Delta t = 180$ seconds to better resolve the fast convective processes .

*b. Observed SST profile and the imposed surface latent heat flux*

To provide a constant surface latent heat flux for the simple (3.5 layer) zonally symmetric monsoon model used here, we mimic the observed SST over the Indian Ocean during boreal summer. More precisely, the discrepancy between the boundary layer saturation equivalent potential temperature and the background boundary layer equivalent potential temperature, in the model, is set to match the observed SST profile. Its strength is set so that its meridional average is 10 K, corresponding to the value used to set a radiative convective equilibrium (RCE) for linear wave analysis of the multicloud model (Khouider and Majda 2006; Waite and Khouider 2009). We used a 35-year (1981/12 to 2016/12) monthly means of SST data from NOAA optimum Interpolation (OI) SST V2 data product (Reynolds et al. 2002), provided by the NOAA/OAR/ESRL PSD, Boulder, Colorado, USA, from their website at http://www.esrl.noaa.gov/psd/. The SST value over the land is obtained by a Cressman interpolation. In order to investigate SST over the Indian Ocean region, all SST values are averaged over the longitude range 60° E – 90° E at different seasons. The resulting profiles are plotted in Figure 1(a). Figure 1(b) shows the imposed surface latent flux profile. The horizontal black line marks the benchmark-RCE value.

## 3. Northward propagating intraseasonal signals and monsoon-like climatology

As summarized in Table 3 the multicloud parameterization employs a large set of parameters. Compared to the standard values established in Khouider and Majda (2006) and Waite and Khouider (2009), only two particular parameters have been tuned here to reach a realistic looking climatological mean circulation with significant intraseasonal variability, namely, the congestus adjustment coefficient which is set to $\alpha_c = 0.22$ (the default is $\alpha_c = 0.25$) and the ratio of moisture at top of the ABL and the mid-tropospheric moisture which is set to $\kappa = 1.25$ (the default is $\kappa = 2$). Starting from a state of rest initial conditions, the equations are integrated for $\sim 1019$ days (to time $t = 3000$ in non-dimensional units). The solution reaches an a statistical equilibrium state within the first 50 days. Conservatively, the analysis results presented herein are based on the last 500 simulation data.

### *a. Northward propagation*

In Figure 2, we show the Hovmöller diagrams (latitude-time contours) of precipitation during both the first 50 days transient period and during the statistical equilibrium period 910-985 days. As we can see after a transient period of 20 days or so the dominant precipitation signals get organized into propagating streaks that start near the equator and move northward and die right before they reach the 20° latitude coinciding with the point where the imposed surface latent heat flux in Figure 1 plunges down. The precipitation streaks repeat roughly every 20 days corresponding to an average propagation speed of $1°\text{day}^{-1}$ (or 1.29 m $\text{s}^{-1}$) consistent with observed BSISO variability. A closer look reveals that the propagation is actually not constant but undergoes a regime change, which goes through two main phases. The precipitation signal begin moving at low latitudes below 10°, at roughly $0.53°\text{day}^{-1}$ and then suddenly accelerates and its speed becomes $1.12°\text{day}^{-1}$ as indicated by the dashed lines in Figure 2(a). While such regime change is not justified by the flat $\Delta_s \theta_e$ profile in Figure 1 and perhaps not yet elucidated in observations, it is important for understanding the northward propagation mechanism; This is one of the main goals here as it is the focus of Section 4.

Figure 2(c) displays the power spectrum of precipitation in the frequency (meridional) wavenumber domain. There is a clear dominant spectral peak at 20 day period corresponding to the BSISO like signals in panel (a) but there are also weaker signals at discrete frequencies which are signatures of a direct cascade of energy toward smaller scales due to quadratic nonlinear interactions between the various modes of the model. The dominant signal of 20 days period interacts with itself to produce a 10 days period signal, which in turn interacts with the 20 day period signal to produce a $1/(1/10+1/20) = 6.667$ day signal (the third horizontal strike from the bottom) while the interaction of the 10 day signal with itself produces a 5 day signal, and so on.

We now average in time the numerical solution over the last 500 days of simulation, between 519 and 1019 days, to obtain a climatological background. This background is then removed from the original time dependent solution to reveal the fluctuations. Figure 3 shows Hovmöller diagrams for the fluctuations of all the prognostic model variables listed in Table 1 as well as the three heating rates, $H_c, H_d, H_s$, corresponding to congestus, deep, and stratiform cloud types, with the precipitation contours (in black) overlaid on top of each panel. The name of the variables are indicated on top of each panel. The BSISO-like signal is evident in all zonal velocity fields, including the ABL, the barotropic, and the first and second baroclinic meridional velocity anomalies. However, the barotropic meridional velocity is very week while $v_b$ is dominated by high frequency signals moving in the opposite direction to the main BSISO signal.

The BSISO signal is strongly dominant in the moisture, $q$, deep convective heating, $H_d$, and stratiform heating panels, which are perfectly in phase with precipitation. Because of the slow propagation speed, the imposed 3 hour lag between stratiform and deep convection becomes insignificant. Congestus heating presents a negative anomaly along the precipitation path as expected from its design to be disfavored to the advantage of deep convection when the atmosphere is moist. Congestus heating is active during the suppressed phase of the BSISO signal and appears to be carried by the high-frequency/fast moving waves seen in the $v_2$ and $\theta_2$ panels which are also dominant in the $\theta_{eb}$ and $\theta_b$ anomalies. In essence, the $\theta_{eb}$ fluctuations triggers the streaks in congestus heating, when the atmosphere is dry, which in turn drive $\theta_2$ and consequently second baroclinic moisture convergence anomalies. However, because the fast waves seem to also weakly precipitate (as seen in the $H_d$ panel), this second baroclinic convergence is not a siginificant driver of moistening during the mature phase of the BSISO wave, which is dominanted by large scale first baroclinic convergence consistent with observations (Hohenegger and Stevens 2013). Nonetheless, as we will see bellow, congestus precoditioning plays a central role during the initiation phase of the BSISO signals near the equator. In Figure 3, there is a clear large-scale signature of $\theta_{eb}$ which leads the BSISO precipitation, an evidence of ABL preconditioning prior to deep convection, consistent with observations (e.g, Kiladis et al. 2009). In the equatorial region, this preconditioning occurs several days prior to the initiation of the BSISO event.

A noticeable feature in the streaks of zonal wind component is the positive barotropic shear vorticity, which can be surmised from the westerly wind lagging south of the easterlies. Though this cyclonic vorticity gets compensated by contributions from the first and second baroclinic vorticities. The former is negative in the upper troposphere while the latter is negative in the lower and upper troposphere according to their respective $\cos(z)$ and $\cos(2z)$ profiles. The presence of the cyclonic barotropic vorticity is consistent with the simulation of Drbohlav and Wang (2005), arguably, in their case, the positive vorticity doesn't get compensated with the second baroclinic mode, since their model doesn't have one. Drbohlav and Wang (2005) argue that this positive vorticity constitutes the main mechanism for northward propagation by inducing barotropic convergence of moisture within the ABL, however, as we can see from Figure 3 the large scale signature is very weak in both $v_b$ and $v_0$, so clearly this is not the mechanism at work in the present model. The main mechanisms will be discussed in Section 4, as already anticipated.

### *b. Circulation patterns and dynamical evolution of the BSISO signals*

We now turn into the dynamical structure of the BSISO-like signal. We begin by plotting in Figure 4 the structure of the total solution during the early stage of the simulation, focusing on the first event that propagates, all the way, northward, seen roughly between times 20 and 40 days in Figure 2(b). We note that the total dynamical fields have been recovered according to the expansions in (2) and (3) and the total heating is accordingly defined as $\mathcal{H} = H_d\sqrt{2}\sin(z) + (H_c - H_s)\sqrt{2}\sin(2z)$. The free tropospheric profiles are augmented below by their ABL counterparts. Notice the black horizontal line on 5 of the panels which marks the ABL top interface and the continuity of the fluid mechanics across this interface.

As we can see from Figure 4, the northward propagating BSISO waves has the following characteristics.

1. Positive moisture anomalies are in phase with precipitation and total heating (e).

2. The diabatic heating is top heavy and slightly skewed southward, a signature of stratiform heating trailing deep convection (e), as in equatorial tropical convective systems (Kiladis et al. 2009; Khouider 2018).

3. A $\theta_{eb}$ anomaly which is slightly leading the convection center, though there is a stronger $\theta_{eb}$ peak south of the main signal, between 5 and 6 degrees, which is accompanied by a much weaker precipitation event (e).

4. Upper tropospheric anti-cyclonic shear vorticity leads the upward motion (a).

5. A backward tilted meridional velocity profile resulting in lower tropospheric convergence and upper tropospheric divergence, which is highly asymmetric with much stronger winds south of the convection center (b).

6. The vertical velocity is in phase with the precipitation maximum and presents a front to rear tilt consistent with the meridional velocity profile (d).

7. Low pressure at low level (f) and positive temperature anomalies below negative temperature anomalies (c) lead the wave.

In Figure 2, we plot the climatological mean flow fields in the latitude-height diagram based on the last 500 day model output. As shown on the panels a,b, and d, there is a counterclockwise circulation cell in the middle to upper troposphere with strong upward motion between the equator and 10°N followed by a weak downward motion in the Southern Hemisphere. This circulation cell is reminiscent of the local Hadley circulation which characterizes the Indian summer monsoon. The total heating in panel (e) is top heavy, somewhat more than the propagating event in Figure 4, indicating the significant contribution from stratiform heating to the mean. The potential temperature mean anomaly is warm in the lower troposphere and cold in the upper troposphere, especially between latitudes $-20°$ and $+30$ °, consistent with the individual event structure in Figure 4. A region of low-level low pressure, at high latitudes of the Northern Hemisphere, marks a monsoon-like trough climatology. The mean free-tropospheric water vapor is characterized by two strong jumps one at 20° S and one at 20° N and a progressive northward sloping in between to reach its maximum near 20° N. Unlike the individual event, the mean moisture maximum is not collocated with the mean precipitation maximum. The accumulation of moisture at Northern latitudes can be attributed to the strong northward mean meridional velocity dominating the lower troposphere between roughly 10° S and 10° N. The mean zonal velocity is mainly barotropic with a baroclinic signature and a double reversal from westerlies to easterlies to westerlies, in the Northern Hemisphere consistent with the southerly wind shear shear prevailing over the summer Indian monsoon trough.

A composite of the anomalous flow fields, with respect to the mean circulation shown in Figure 5, is presented by the panels of Figure 6. To obtain the composite solution, we averaged the flow anomalies along the curve in the space-time domain following the precipitation maximum, between days 935 and 955, i.e, focusing on the corresponding propagating event in Figure 2(a). As we can see, this anomalous wave disturbance has many common features with the total solution in Figure 3 but it has also a few major differences. Among the common features we can enumerate the correlation of precipitation with anomalous moisture perturbation and $\theta_{eb}$ anomalies (although weak, note the 0.1 K units) leading moisture anomalies. As we will see below despite this fact, the leading increase of $\theta_{eb}$ anomalies does not cause northward propagation, simply because they are too weak to drive the precipitation anomalies; moisture does. The skewed $\theta_{eb}$ profile is a consequence of ABL drying due to stratiform induced downdrafts in the wake of the wave. We also have a backward tilted meridional and vertical velocity fields with convergence below and divergence aloft and upward motion in phase with the convection. However, unlike the total wave solution in Figure 2, there is a significant positive shear vorticity in the middle troposphere, though it is far from being simply barotropic.

There is a significant capping by negative vorticity near the top of the domain. The meridional wind appears to be less asymmetric and even somewhat stronger in the northern half of the wave. The potential temperature plot features anomalously warm air topper by cold air north of the convection center while warm temperature sits on top of cold temperature within the convection center. This feature is consistent with equatorial convectively coupled waves and the MJO (Kiladis et al. 2009; Khouider 2018). Moreover, form panel (f), we have a positive pressure perturbation below a negative one ahead of the wave backed by low-level low pressure and upper level high pressure in hydrostatic balance with the potential temperature in panel (c). This indicates in particular that the wave is mainly baroclinic in nature and the barotropicity is all carried by the mean flow. So the build up of the positive barotropic vorticity in front of the wave (if there is one) cannot be the driver of the northward propagation as it has been reported in many publications.

There is no doubt that the environment plays a role in the wave motion; if the wave could propel itself it cannot be through the buildup of positive barotropic vorticity. A more appropriate mechanism will be discussed below after we present a detailed budget analysis for the moisture and meridional momentum equations. Contrarily, to the mean driven wave fluctuation point of view, our analysis below is based on the full nonlinear wave-solution and the physics of the wave fluctuation (in Figure 5) alone cannot to lead to same conclusive arguments. The mean flow-wave interaction plays a central in the mechanisms proposed here for BSISO initiation, propagation, and termination. Arguably, the its is the wave aggregate that make the mean and not the opposite.

## 4. Propagating mechanism of northward-moving precipitating events

### *a. Moisture budget analysis*

The governing equation for vertically integrated moisture, in the free troposphere, is given on the 10th row of Table 1.

In Figure 7, we plot the profiles of all the tendency terms for the free-tropospheric moisture for two different events, one corresponding to an early stage of the BSISO event when it is still near the equator, below 10° N (slow propagation regime) and the other at higher latitudes, above 10° N, when the BSISO propagation speed gets accelerated (fast propagation regime). We note that the nonlinear moisture flux terms have been divided into convergence, $q\partial v_j$ and advection, $v_j\partial q,\ j = 0,1,2,$ terms. Before digging into differences between these two cases, we focus on some of the main common features. In both cases, the total time tendency (thick black curve) of moisture $\frac{\partial q}{\partial t}$ is characterized by positive anomalies to the north and negative tendency to the south of the precipitation maximum (thick red curve), which is consistent with the northward propagation of the wave disturbance. The main moisture source comes from the terms, $-q\frac{\partial(\tilde{\alpha}_1 v_1)}{\partial y}$

and $-\frac{\partial(\tilde{Q}_1 v_1)}{\partial y}$, corresponding to first baroclinic convergence of moisture anomalies and moisture background, respectively. The combination of these two terms by themselves balance the sink of moisture due to precipitation as they seem to be perfectly in phase with it. We notice that barotropic convergence (thin pink line) is practically zero and the second baroclinic convergence is interestingly a moisture sink. The later is due to the prevalence of stratiform heating which induces low-level divergence in the second baroclinic mode. The meridional profiles of all moisture convergence terms are perfectly symmetric about the maximum precipitation. Thus moisture convergence by either barotropic or baroclinic modes cannot be the reason for the northward propagation of the moisture disturbance and ultimately the convectively coupled wave.

In addition to second baroclinic divergence and precipitation, the major moisture sinks include meridional advection $-v_1 \frac{\partial(\tilde{\alpha}_1 q)}{\partial y}$. Among these three processes, only the first baroclinic meridional advection term shows substantial meridional asymmetry to be able to induce the northward propagation of moisture anomalies. Thus, we argue that the latter is the main physical mechanism that induces northward propagation the BSISO signals in the present model simulation mainly through the intrusion of relatively dry air from the southern flank of the convection center forcing the whole system to move northward where the environment is less hostile for new convection. We note that the curves in Figure 7 correspond to the total budget terms and not anomalies and that the advection asymmetry is consistent with the asymmetry of the meridional velocity seen in Figure 4, which asymmetry is inexistent in the fluctuation composite in Figure 6. Comparing panels a and b in Figure 7, we can see that the main difference is the magnitude of the first-baroclinic meridional advection asymmetry. The latter is much more significant in panel b consistent with the fact that the wave moves faster north of 10° N.

To dig a bit deeper into this issue, we plot in Panels a and b of Figure 8 the meridional profiles of total moisture gradient and total first-baroclinic meridional velocity (solid lines) and their respective climatological means (dashed lines) for the cases when the BSISO wave is, respectively, bellow 10° N and when it moves beyond this latitude. In the low latitude case in Figure 8a, the meridional profile of total moisture is mostly symmetric about the precipitation center, while that of meridional velocity is asymmetric with strong southerlies to the south and weak northerlies to the north. As already anticipated, such strong southerlies south of the precipitation maximum bring dry air into the convection core and force convection move to the north. In Fig.8b on the other hand, the $v_1$ asymmetry is much stronger while the meridional gradient of moisture also shows some asymmetry. The asymmetry in the moisture gradient is attributed to the persistence of a background moisture gradient in the mean climatology at those latitudes, consistent with the mean moisture profile in Figure 5; the climatological mean moisture gradient in panel (a) is relatively much weaker however the mean $v_1$ velocity is significant and overall positive, contributing to the asymmetry in the total meridional wind around the precipitation maximum.

Previous studies (Jiang et al. 2004; Drbohlav and Wang 2005, 2007) had emphasized the role of positive barotropic vorticity anomalies in inducing barotropic convergence which translates into ABL moisture convergence, north of the convection center and eventually lead to the northward propagation of precipitation. To check this hypothesis more closely, we plot in Figure 8c-d the meridional profiles of vorticity and divergence anomalies. It is particularly interesting to note that the barotropic vorticity $-\partial_y u_0$, does have about 0.7 degree northward lead in panel (c) but it is mainly in phase with the precipitation maximum in panel (d). If at times barotropic cyclonic vorticity may appear to lead the northward moving BSISO signals, this feature is not as universal the the asymmetry in the advecting $v_1$ wind reported above. More importantly, the barotropic wind divergence is close to zero, thus the ABL convergence mechanism is not present here.

To further show evidence of the relevance of the first baroclinic velocity for the northward propagation of the BSISO events, we introduce the average first baroclinic meridional velocity in the vicinity of the precipitation maximum corresponding the northward propagating BSISO events, as

$$\bar{v}_1(y_t) = \frac{1}{y_0}\int_{y_t-y_0/2}^{y_t+y_0/2} v_1(y,t)\,dy, \tag{4}$$

where $y_t$ is the point of maximum precipitation and $y_0 = 4.65°$is a fixed averaging range.

In Figure 9(a)-(c), we plot the aggregated time mean corresponding to all BSISO events that occurred during the last 500 days of the simulation, roughly 25 events, as a function of latitude, i.e, $y_t$ with the mean propagation speed of the BSISO at the corresponding location, the time lag correlation of $\bar{v}_1(y_t)$ and the BSISO propagation speed, $s(y_t)$, and a scatter plot of $\bar{v}_1(y_t)$ with respect to $s(y_t)$. While there is some scattering, it is clear from this figures that these two variables are well correlated and the regime change of the northward propagation speed as the BSISO passes beyond some latitude point near 10°N is reflected in the inflection point (a point of minimum speed) seen near 8°above which both $\bar{v}_1$ and $s$ accelerate to reach its maximum near 14°. We note that $\bar{v}_1$ plunges down first, before the BSISO event terminates at roughly 17°. The latter is somewhat reflected in the lag correlation plot in panel (b) which is, although maximized at $\tau = 0$, highly skewed towards negative lag values hinting to the causal effect of $\bar{v}_1$ on $s$.

To understand the origin of this asymmetry in meridional wind, we turn into the analysis of the meridional momentum equations. Namely, we will investigate which physical parameter is at the origin of the asymmetry in the first baroclinic velocity component. According to our experimental setting, including the SST profile in Figure 1, which is totally flat between latitudes -10° and 20° , containing the region where the BSISO event evolve, the only physical parameter susceptible to induce an asymmetry in $v_1$ is the beta effect. Next, we demonstrate that this is indeed the case in the context of a simple linear dynamical model with an imposed heat source.

*b. Role of beta-effect in inducing northward propagation*

We consider the linear first baroclinic shallow water equations with an imposed heat source mimicking the convective heating emanating from the BSISO events, which are otherwise completely decoupled from all the other vertical modes, including the ABL. We have

$$\begin{aligned} u_t - yv &= -\alpha u, \\ v_t + yu &= \theta_y - \alpha v, \\ \theta_t - v_y &= Q(y) - \alpha\theta, \end{aligned} \tag{5}$$

where $u, v, \theta$ are the zonal velocity, meridional velocity, and potential temperature. Here $Q(y)$ is the imposed heat source having the shape of a Gaussian: $Q(y) = q_0 e^{-((y-y_0)/L_y)^2}$, where $q_0$ is the strength of the heating, $y_0$ its center and $L_y$ its decaying scale and $\alpha^{-1} = 50$ day$^{-1}$ is a small damping coefficient taking to be the same for all three equations, for the sake of convenience. We set $y_0 = 10°$ and $L_y = 0.13°$, leading to an effective decay in the heat source of about 2 degrees, while $q_0 = 20$ K day$^{-1}$ consistent with the results in Figures 2, 4, and 6(e). Eliminating $u$ and $\theta$ from (5) leads to the following wave-like equation for $v$.

$$\partial_{tt} v = \partial_{yy} v - (y^2 + \alpha^2)v - 2\alpha\partial_t v + \partial_y Q. \tag{6}$$

This equation is then solved numerically with centered differences, using homogeneous Dirichlet boundary conditions ($v = 0$). In Figure 10 we plot the solution after 200 days of integration on top of its counterpart when the Coriolis parameter is set to zero, i.e, the term $y^2 v$ on the right hand side is dropped. As we can see, the main difference between the two solutions is that the former is asymmetric about the heating center while the latter is perfectly symmetric. The explanation for this behavior is embarrassingly simple. The Coriolis term $y^2 v$ acts as an extra damping term for the solution. Since $y$ is larger to the North, there is more damping there. Also shown in Figure 10, for the value of the average $\bar{v}$, which turns out to be about 0.85 m s$^{-1}$, a value comparable to the typical propagation speeds achieved by the solution in Figure 9.

It is worthwhile noting that the solution in Figure 10 is quantitatively sensitive to the domain size at the location of $y_0$ and more importantly to the damping rate but it remains qualitatively robust, as long as the two boundaries are kept at an equal distance from the heat source. Because of the complex nonlinearity in the multicloud model, as seen in Table 1, it will be hard to draw more analogies with the Northward propagation of the BSISO signals presented here besides the fact that the asymmetry in $v_1$ originates from the asymmetry in the damping effect. Obviously, in a full 2d model the Coriolis effect will simply transfer energy from the meridional velocity into the zonal propagating waves instead of dissipating it but the end result will most likely be similar as more energy will be drawn out $v$ at higher latitudes, i.e, North of the convection center, because Poincaré waves with the same wavenumber would have higher frequencies at larger $f(=\beta y)$ parameter values.

### *c. Cause and effect of northward propagation*

We now summarize the main physical processes leading to northward propagating of the BSISO anomalies. (1) Northward propagation is due to the northward movement of moisture anomalies due to interplay between the symmetric convergence of moisture, which its itself results from the induced convective heating, and the asymmetric moisture advection. (2) The asymmetric meridional advection by the first-baroclinic meridional velocity induces dry air intrusions to the south of moisture anomalies, which make the southern flank of the anomaly unfavorable to new convection, hence convection is shifted northward. (3) The asymmetric meridional advection is mainly contributed by the asymmetric first-baroclinic meridional velocity $v_1$, especially at low latitudes. (4) The asymmetry in $v_1$ results from the beta effect as gravity waves are damped at a higher rate north of the disturbance; This may seem an artifact of the zonally symmetric setting as illustrated above. In a more realistic three dimensional setting, Poincaré waves at higher latitudes have higher frequencies especially those with small zonal wavenumbers. As such energy will be transferred more quickly to smaller scales and thus dissipated at a higher rate.

## 5. Initiation and termination of BSISO events

Another issue of great interest is the initiation of the BSISO events in the vicinity of the equator. As shown in Figure 3, positive precipitation anomalies are generally triggered at low latitudes of the Northern Hemisphere as the preceding northward propagating BSISO terminates at high latitudes. Through moisture budget analysis, once again, we would like to figure out the dominant effects that cause the triggering and intensification of convection at low latitudes of the Northern Hemisphere.

Figure 11(a) shows the moisture budget analysis where all terms appearing in the free tropospheric moisture equation are plotted separately at functions of time. To obtain smooth signals we have taken averaging about the latitude range between the equator and 5° N. We focus on the period $-15$ days and $+6$ days, relative the maximum precipitation. As shown by the bold black line, the time tendency of moisture $\frac{\partial q}{\partial t}$ reaches its maximum value one day before the maximum precipitation and has negative value after the maximum precipitation. Form Figure 11(a) we can see that the main dominant terms (excluding $S^q$, which all the way constant) are the first-baroclinic moisture convergence, associated with both moisture anomalies $-q\frac{\partial(\tilde{\alpha}_1 v_1)}{\partial y}$ and background moisture $-\frac{\partial\left(\tilde{Q}_1 v_1\right)}{\partial y}$ terms, the second-baroclinic moisture convergence $-\frac{\partial\left(\tilde{Q}_2 v_2\right)}{\partial y}$, and precipitation $\mathcal{P}$ as well as the term $S^q$ which provides a constant source of moisture. In terms of their phase relation, all these dominant terms are more or less in phase with the maximum precipitation but the second baroclinic convergence (thin magenta line) which peaks some 5 days ahead of the precipitation maximum. While it doesn't seem to induce a positive moisture tendency at this early stage, it does compensate, together with $S^q$, for the moisture sink due to the first baroclinic moisture divergence and precipitation.

In Figure 11(b), we make similar plots for the deep, congestus, and stratiform heating rates, $H_d, H_c, H_s$, as well as the moisture and different components of potential temperature anomalies. Deep heating $H_d$ is mostly in phase with moisture $q$, although the maximum moisture does lag the maximum deep heating slightly. Besides deep heating, stratiform heating $H_s$ reaches maximum strength at almost the same time as deep heating, which should be related with the fact that the stratiform heating lags deep heating through a relaxation time scale of only 3 hours. We note that congestus heating $H_c$ is generally suppressed and nearly vanishes during the deep heating period but is active, reaching up to 0.25 K day$^{-1}$, the rest of the time, when deep convection is suppressed. As for potential temperature anomalies, low boundary layer equivalent potential temperature anomalies $\theta_{eb}$ are induced during precipitation, while the boundary layer potential temperature $\theta_b$ has warm anomalies. Such low boundary layer equivalent potential temperature anomalies are induced by the downdrafts that tend to dry the ABL. Furthermore, both the first and second-baroclinic potential temperature anomalies $(\theta_1, \theta_2)$ lead the maximum precipitation. However, positive first-baroclinic potential temperature anomalies $\theta_1$ lead the first increase in precipitation, before day $-5$. This is essentially a stabilizing mechanism and thus temperature anomalies cannot be attributed the role of initiating the BSISO events.

The negative first-baroclinic potential temperature anomalies are induced though kinetic dynamics while the deep convective heating is merely compensated by convergence as it can surmised from Figure 11(b), which shows meridional profiles of vorticity and divergence fields in the barotropic and first- and second-baroclinic modes. It is interesting to notice that there are positive barotropic vorticity anomalies $-\frac{\partial u_0'}{\partial y}$ two days before the maximum precipitation, although the barotropic divergence field $\frac{\partial v_0'}{\partial y}$ shows negligible magnitude. As for the baroclinic mode, there are negative first-baroclinic vorticity anomalies preceding the maximum precipitation. More importantly, second-baroclinic convergence with comparable first-baroclinic divergence precedes the intensified precipitation. The second baroclinic convergence is maintained by the background congestus heating.

Figure 12a-b shows a life cycle of one BSISO event starting from its initiation into a big blurb of convection near the equator until it reaches relatively high latitudes. We note in particular that during the initiation phase (panel a), when the dominant event is still at the equator, there is a secondary peak in precipitation at roughly 17° N. The latter is a signature of the termination phase of the preceding BISO event. Moreover, we note that as the main event propagates Northwards, it starts inducing subsidence near and south of the equator suppressing the intensification of convection there. However, as this event moves far enough from the equator, equatorial convection starts to intensify (panel f) before it becomes again dominant (panel a) and the cycle is closed.

Before we address the issue of termination of the BSISO events, we summarize here the processes leading to the initiation of BSISO convection near the equator. (1) During suppressed phase, the first-baroclinic divergence and second-baroclinic convergence cancel each other, resulting in a vanishing moisture convergence. (2) The first-baroclinic divergence near the equator is a maintained by the intensification of the local Hadley circulation due to the northward-moving precipitating event when it moves to higher latitudes. (3) Once the propagating event moves to higher latitudes and terminates, the first-baroclinic divergence near the equator weakens and the second-baroclinic convergence, which is maintained by the background congestus heating, becomes dominant, resulting in moisture convergence and precipitation intensifies, via a positive feedback loop.

The panels (a) and (b) of Figure 13 show the moisture budget analysis, all terms appearing in the free tropospheric moisture equation, at two successive instances during the BSISO life cycle, a few days before its termination. Not surprisingly, the plots in Panel (a) are very similar to those in Figure 7(b), though redundant, they are kept here to ease the comparison between the mature phase of the BSISO event, represented by Figures 7b) and 13(a), and the time when BSISO event moves to higher latitudes and weakens, represented by Figure 13(b), before it terminates. Notice the weakening the moisture total tendency north the convection center and the apparent negative tendency in the vicinity of the precipitation maximum, marked by the vertical dotted line, in Panel (b). Beside this observation, the striking difference between the two panels in Figure 13 resides in the significant reduction in the (asymmetric) advection of dry air towards the center and more importantly the relatively strong first baroclinic divergence north of the convection center seen in Panel (b). Moreover all the tendency signals are much weaker at that time (notice the change in scale between Panels a and b. The weakening of moisture convergence is probably caused by a weakening of precipitation as the mean moisture gradient starts to decay towards the negatives, as seen in Panel (d) in comparison with Panel (c). As such the total moisture tendency is much weaker in front of the wave when the BSISO event moves at high latitude as it approaches the edge of the warm SST background which plunges down at exactly 20° N. As also seen in Figure 13(d), the asymmetry argument in $v_1$ is still valid, however, the weakening of the whole waves makes the average $\bar{v}_1$ in (4), if it were computed, much weaker, which translates into the stalling of the BSISO event and consequently causing its demise through further weakening via moisture depletion by precipitation. This in part explains why the BSISO events do not quite reach the 20° N SST barrier before weakening and terminating.

## 6. Concluding discussion

This paper is aimed at modeling the northward-moving BSISO events over the Indian monsoon region from a zonally symmetric perspective. Specifically, we use a nonlinear free-tropospheric model coupled to the multicloud parameterization with ABL dynamics of Waite and Khouider (2009) to simulate the northward-moving BSISO events, in order to gain basic understanding about the underlying basic physical mechanisms. The model is based on the zonally symmetric primitive equations, Galerkin projected onto the first three modes of vertical structure: the barotropic mode and the first two baroclinic modes, and it is dynamically and thermodynamically coupled to a bulk (vertically averaged) ABL dynamics. The numerical procedure followed here and its validation as well as it suitability for simulating the monsoon flow are found in De La Chevrotière and Khouider (2017). Zonally symmetric models have been used in the past to steady for example, , as in our case, the northward propagation of monsoon precipitation (Drbohlav and Wang 2005) and for the effect of the ABL dynamics on the Hadley cell (Pauluis 2004). Because of its resemblance to the Asian monsoon, the model and results presented here could be applied to the North American monsoon as well (Jiang and Waliser 2009; Jiang and Lau 2008).

The model is forced with an imposed surface latent heat flux based on the observed SST profile over the Indian Ocean summer (JJA) climatology and integrated for roughly 1000 days. Northward propagating BSISO events, regularly succeeding each other at a period of roughly 20 days and moving at roughly $1°\text{day}^{-1}$, as in observations, start to appear after a transient period of nearly the same length.

In addition to the 20 days period and the $1°\text{day}^{-1}$ propagation speed, the BSISO events have many realistic features, including moisture convergence in phase with the precipitation maximum, a top heavy heating slightly tilted southward as a result of stratiform heating which slightly lags deep convection, ABL moisture slightly leading, upper level shear vorticity lead the wave, a backward tilted meridional velocity with convergence below divergence aloft ,more or less in phase with precipitation, resulting in a tilted upward motion in phase with precipitation, and finally low pressure at low level leading the wave. While these circulation features are more or less in agreement with equatorial waves dynamics, where the tilted structure is believe to lead to wave propagation, a thorough moisture budget analysis revealed that the main mechanism responsible for the northward propagation is due to the intrusion of dry air from the southern flank of the wave induced by an asymmetry in the first baroclinic meridional velocity. Although dry air is advected from both ends of the convection center, the asymmetry in $v_1$ is such that more dry air is pumped from the southern side making the northern side more favorable to new convection and thus making the whole disturbance move to the North. We also found that precipitation itself is nearly balanced by moisture convergence, so moisture advection is the sole mechanism responsible for the wave propagation as we found that the $v_1$ asymmetry is statistically correlated with the BSISO propagation speed.

To understand the cause of the asymmetry in the $v_1$ velocity we introduced a toy model reduced to the zonally symmetric first baroclinic mode with an imposed heating. As demonstrated in Figure 10, the beta effect alone explains this asymmetry by acting as an asymmetric damping diminishing the strength of the flow response north of the heat source. While the beta damping itself is obviously an artifact of the zonal symmetry, in a fully three dimensional model this can be contrasted by the fact that zonally propagating Poincaré waves, north of the heat source, have higher frequencies than those south of the heat source, because of the larger $f$ parameter there, thus becoming more effective in transferring energy down to (turbulent) dissipation scales.

Jiang et al. (2004) has proposed the generation of barotropic shear vorticity due to the interactions between the free-tropospheric baroclinic and barotropic modes and the mean flow as the main mechanism for Northward propagation by inducing ABL convergence indirectly through the production of upper level divergence. In this paper, although both the vertical shear of the mean flow (see Figure 5) and the northward displaced barotropic vorticity (see Figure 8c) are (sometimes) captured, the induced barotropic vorticity does not cause barotropic divergence in the free troposphere nor moisture convergence in the ABL. They also have emphasized the role of moisture-convection feedback induced via two distinct processes. One of them is moisture advection by the mean southerly in the ABL, which is not significant here as the intraseasonal variability is quite weak in the ABL (see Figure 4). The other one is moisture advection due to mean meridional specific humidity gradient, thus implying dry air intrusion from the south just like in our case. Although the mean moisture gradient does exhibit a northward increasing gradient, as shown in Figure 7, the major source of asymmetry comes from the asymmetry in the first-baroclinic meridional wind, rather than moisture gradient. In fact, our initial set up is a radiative convective equilibrium with a uniform moisture background. So the moisture background seen in Figure 5(e) is a result of the wave activity and not its cause. As we can see from Figure 2(b), convective events begin to propagate away from the equator as soon as they form at day 0. All the background seems to imply is the inhibition of new convection south of the equator. This is further evidence that the beta induced asymmetry plays the key role in the northward propagation of BSISO events.

We also looked at the mechanisms of initiation near the equator and terminations near 20° N of BSISOs. Our investigation reveals that initiation of new BSISO events is mainly triggered by the second baroclinic moisture convergence induced by an omnipresent congestus heating background, in the equatorial region, which fades only during and within the active phase of the BSISO events. While this second baroclinic convergence is over-compensated by the first baroclinic divergence associated with the pre-existing actively propagating BSISO event north of the equator, through the intensification of the local Hadley circulation, it becomes dominant and lead to an intensification of equatorial convection as soon as the preceding BSISO event reaches high enough latitude and terminates. This is somewhat consistent with the Hadley cell-wave interaction mechanism suggested by Wang and Xie (1997).

As for the termination, we found that it starts by the weakening the wave as it approaches the edge of the imposed warm SST profile leading to a weakening of the first baroclinic meridional velocity and its asymmetry measure, thus nearly stalling the wave and making it vulnerable to precipitation induced drying and further weakening.

The BSISO events as seen in Figure 2 are indeed too regular. An easy way to break this regularity and simulate BSISO events with some intermittency behavior as in nature, one could use the stochastic version of the multicloud parameterization (Khouider et al. 2010; Frenkel et al. 2012), which is based and birth-death lattice model and has been implemented and successfully in general circulation models (e.g Deng et al. 2015; Goswami et al. 2017b). In fact, De La Chevrotière and Khouider (2017) has already implemented this stochastic parameterization scheme in this zonally symmetric model, however, our first test with this model were unsuccessful in producing cleanly visible northward propagating BSISO although as shown in De La Chevrotière and Khouider (2017) such signals are there but the noisy-ness of the simulation made it hard to analyze. With the understanding gained here, we conjecture that the inconclusive results are due to the fact that strong stochastic fluctuations may have prevented the asymmetry in $v_1$ to persist at the BSISO scale. This can be easily verified by tuning down the stochastic noise by increasing the number of lattice sites for example. Moreover, an important future research direction is to test these conclusions in a full 3d setting by either running the same model where the zonal symmetry is relaxed or using cloud permitting simulations.

*Acknowledgments.* The research of B.K is partially funded by a Discovery grant from the Natural Sciences and Engineering Research Cancel of Canada. This research was done when Q.Y. was visiting the University of Victoria during the months of September to December 2017. This research of A.J.M. is partially supported by the Office of Naval Research ONR MURI N00014-12-1-0912 and the Center for Prototype Climate Modeling (CPCM) in New York University Abu Dhabi (NYUAD) Research Institute.

## References

Ajayamohan, R. S., B. Khouider, and A. J. Majda, 2013: Realistic initiation and dynamics of the Madden-Julian oscillation in a coarse resolution aquaplanet GCM. *Geophys. Res. Lett.*, **40**, 1–6, doi:10.1002/2013GL058187.

Ajayamohan, R. S., B. Khouider, and A. J. Majda, 2014: Simulation of monsoon intraseasonal oscillations in a coarse-resolution aquaplanet gcm. *Geophysical Research Letters*, **41 (15)**, 5662–5669, doi:10.1002/2014GL060662, URL http://dx.doi.org/10.1002/2014GL060662.

Biello, J., and A. Majda, 2005: A multi-scale model for the madden–julian oscillation. *J. Atmos. Sci.*, **62**, 1694–1721.

Brunet, G., and Coauthors, 2010: Collaboration of the weather and climate communities to advance subseasonal-to-seasonal prediction. *Bulletin of the American Meteorological Society*, **91 (10)**, 1397–1406.

De La Chevrotière, M., and B. Khouider, 2017: A zonally symmetric model for the monsoon-hadley circulation with stochastic convective forcing. *Theoretical and Computational Fluid Dynamics*, **31 (1)**, 89–110.

Deng, Q., B. Khouider, and A. J. Majda, 2015: The MJO in a coarse-resolution GCM with a stochastic multicloud parameterization. *Journal of the Atmospheric Sciences*, **72 (1)**, 55–74, doi:10.1175/JAS-D-14-0120.1.

Drbohlav, H.-K. L., and B. Wang, 2005: Mechanism of the northward-propagating intraseasonal oscillation: Insights from a zonally symmetric model. *Journal of climate*, **18 (7)**, 952–972.

Drbohlav, H.-K. L., and B. Wang, 2007: Horizontal and vertical structures of the northward-propagating intraseasonal oscillation in the south asian monsoon region simulated by an intermediate model. *Journal of Climate*, **20 (16)**, 4278–4286.

Frenkel, Y., A. J. Majda, and B. Khouider, 2012: Using the stochastic multicloud model to improve tropical convective parameterization: A paradigm example. *J. Atmos. Sci.*, **69**, 1080–1105.

Fu, X., and B. Wang, 2004: Differences of boreal summer intraseasonal oscillations simulated in an atmosphere–ocean coupled model and an atmosphere-only model. *Journal of climate*, **17 (6)**, 1263–1271.

Goswami, B. B., B. Khouider, R. Phani, P. Mukhopadhyay, and A. J. Majda, 2017a: Improved tropical modes of variability in the NCEP Climate Forecast System (Version 2) via a stochastic multicloud model. *Journal of the Atmospheric Sciences*, **74 (10)**, 3339–3366, doi:10.1175/JAS-D-17-0113.1.

Goswami, B. B., B. Khouider, R. Phani, P. Mukhopadhyay, and A. J. Majda, 2017b: Improving synoptic and intraseasonal variability in cfsv2 via stochastic representation of organized convection. *Geophys. Res. Lett.*, **44**, 1104–1113, doi:10.1002/2016GL071542.

Hendon, H. H., and B. Liebmann, 1994: Organization of convection within the Madden-Julian oscillation. *J. Geophysical Res.*, **99**, 8073–8084.

Hendon, H. H., and M. L. Salby, 1994: The life cycle of the Madden-Julian oscillation. *J. Atmos. Sci.*, **51**, 2225–2237.

Hohenegger, C., and B. Stevens, 2013: Preconditioning deep convection with cumulus congestus. *J. Atmos. Sci.*, **70 (2)**, 448–464.

Jiang, X., and N.-C. Lau, 2008: Intraseasonal teleconnection between north american and western north pacific monsoons with 20-day time scale. *Journal of Climate*, **21 (11)**, 2664–2679, URL http://www.jstor.org/stable/26260297.

Jiang, X., T. Li, and B. Wang, 2004: Structures and mechanisms of the northward propagating boreal summer intraseasonal oscillation. *Journal of Climate*, **17 (5)**, 1022–1039.

Jiang, X., and D. E. Waliser, 2009: Two dominant subseasonal variability modes of the eastern pacific itcz. *Geophysical Research Letters*, **36 (4)**, n/a–n/a, doi:10.1029/2008GL036820, URL http://dx.doi.org/10.1029/2008GL036820, l04704.

Jiang, X., and Coauthors, 2015: Vertical structure and physical processes of the madden-julian oscillation: Exploring key model physics in climate simulations. *Journal of Geophysical Research: Atmospheres*, **120 (10)**, 4718–4748, doi:10.1002/2014JD022375, URL http://dx.doi.org/10.1002/2014JD022375, 2014JD022375.

Johnson, R. H., T. M. Rickenbach, S. A. Rutledge, P. E. Ciesielski, and W. H. Schubert, 1999: Trimodal characteristics of tropical convection. *Journal of Climate*, **12 (8)**, 2397–2418.

Kemball-Cook, S., and B. Wang, 2001: Equatorial waves and air–sea interaction in the boreal summer intraseasonal oscillation. *Journal of Climate*, **14 (13)**, 2923–2942.

Khouider, B., 2018: *Models for Tropical Climate Dynamics: Waves, Clouds, and Precipitation*. Springer, New York, 300 pages pp.

Khouider, B., J. Biello, A. J. Majda, and Coauthors, 2010: A stochastic multicloud model for tropical convection. *Communications in Mathematical Sciences*, **8 (1)**, 187–216.

Khouider, B., and A. J. Majda, 2005: A non-oscillatory well balanced scheme for an idealized tropical climate model. Part I: Algorithm and validation. *Theor. Comp. Fluid Dyn.*, **19**, 331–354.

Khouider, B., and A. J. Majda, 2006: A simple multicloud parameterization for convectively coupled tropical waves. part i: Linear analysis. *J. Atmos. Sci.*, **63**, 1308–1323.

Khouider, B., and A. J. Majda, 2008a: Equatorial convectively coupled waves in a simple multicloud model. *J. Atmos. Sci.*, **65**, 3376–3397.

Khouider, B., and A. J. Majda, 2008b: Multicloud model for organized tropical convection: Enhanced congestus heating. *J. Atmos. Sci.*, **65**, 895–914.

Khouider, B., A. St-Cyr, A. J. Majda, and J. Tribbia, 2011: The MJO and convectively coupled waves in a coarse resolution GCM with a simple multicloud parameterization. *J. Atmos. Sci.*, **68**, 240–264, doi:101.1175/2010JAS3443.1.

Kiladis, G. N., M. C. Wheeler, P. T. Haertel, K. H. Straub, and P. E. Roundy, 2009: Convectively coupled equatorial waves. *Rev. Geophys.*, **47**, RG2003, doi:10.1029/2008RG000 266.

Lau, W. K.-M., and D. E. Waliser, 2011: *Intraseasonal variability in the atmosphere-ocean climate system*. Springer Science & Business Media.

Lawrence, D. M., and P. J. Webster, 2002: The boreal summer intraseasonal oscillation: Relationship between northward and eastward movement of convection. *Journal of the atmospheric sciences*, **59 (9)**, 1593–1606.

Lee, J.-Y., B. Wang, M. C. Wheeler, X. Fu, D. E. Waliser, and I.-S. Kang, 2013: Real-time multivariate indices for the boreal summer intraseasonal oscillation over the asian summer monsoon region. *Climate Dynamics*, **40 (1-2)**, 493–509.

Madden, R. A., 1986: Seasonal variations of the 40-50 day oscillation in the tropics. *J. Atmos. Sci.*, **43**, 3138–3158.

Madden, R. A., and P. R. Julian, 1971: Detection of a 40–50 day oscillation in the zonal wind in the tropical pacific. *Journal of the atmospheric sciences*, **28 (5)**, 702–708.

Madden, R. A., and P. R. Julian, 1972: Description of global-scale circulation cells in the tropics with a 40–50 day period. *Journal of the atmospheric sciences*, **29 (6)**, 1109–1123.

Majda, A. J., and S. N. Stechmann, 2009: The skeleton of tropical intraseasonal oscillations. *Proc. Natl. Acad. Sci. USA*, **106**, 8417–8422.

Pauluis, O., 2004: Boundary layer dynamics and cross-equatorial hadley circulation. *Journal of the atmospheric sciences*, **61 (10)**, 1161–1173.

Raymond, D. J., 2001: A new model of the maddenjulian oscillation. *Journal of the Atmospheric Sciences*, **58 (18)**, 2807–2819, doi:10.1175/1520-0469(2001)058⟨2807:ANMOTM⟩2.0.CO;2.

Reynolds, R. W., N. A. Rayner, T. M. Smith, D. C. Stokes, and W. Wang, 2002: An improved in situ and satellite sst analysis for climate. *Journal of climate*, **15 (13)**, 1609–1625.

Seo, K.-H., J.-K. E. Schemm, W. Wang, and A. Kumar, 2007: The boreal summer intraseasonal oscillation simulated in the ncep climate forecast system: the effect of sea surface temperature. *Monthly weather review*, **135 (5)**, 1807–1827.

Sikka, D., and S. Gadgil, 1980: On the maximum cloud zone and the itcz over indian, longitudes during the southwest monsoon. *Monthly Weather Review*, **108 (11)**, 1840–1853.

Stechmann, S. N., A. J. Majda, and B. Khouider, 2008: Nonlinear dynamics of hydrostatic internal gravity waves. *Theor. Comp. Fluid Dyn.*, **22**, 407–432.

Waite, M. L., and B. Khouider, 2009: Boundary layer dynamics in a simple model for convectively coupled gravity waves. *J. Atmos. Sci.*, **66**, 2780–2795.

Wang, B., and X. Xie, 1997: A model for the boreal summer intraseasonal oscillation. *Journal of the Atmospheric Sciences*, **54 (1)**, 72–86.

Yasunari, T., 1979: Cloudiness fluctuations associated with the northern hemisphere summer monsoon. *Journal of the Meteorological Society of Japan. Ser. II*, **57 (3)**, 227–242.

Yasunari, T., 1980: A quasi-stationary appearance of 30 to 40 day period in the cloudiness fluctuations during the summer monsoon over india. *Journal of the Meteorological Society of Japan. Ser. II*, **58 (3)**, 225–229.

Zhang, C., 2005: Madden-julian oscillation. *Reviews of Geophysics*, **43 (2)**.

Zhang, C., 2013: ”madden-julian oscillation”: Bridging weather and climate. *Bulletin of the American Meteorological Society*, **94 (12)**, 1849–1870, doi:10.1175/BAMS-D-12-00026.1.

# LIST OF TABLES

TABLE 1. Governing equations for all physical variables in the ABL, barotropic, and first- and second-baroclinic modes in the free troposphere. The notation $\frac{D_0}{Dt} = \frac{\partial}{\partial t} + v_0 \frac{\partial}{\partial y}$ stands for the advection by barotropic meridional velocity and $\frac{D_b}{Dt} = \frac{\partial}{\partial t} + v_b \frac{\partial}{\partial y}$ stands for the advection by the ABL meridional velocity. The momentum and potential temperature differences between two heights are denoted by the notations, $\Delta_s \phi \equiv \phi_s - \phi_b$, $\Delta_t \phi \equiv \phi_b - \phi_t$, $\Delta_m \phi \equiv \phi_b - \phi_m$, where $s, b, m$ represent surface, ABL and middle troposphere respectively. The parameter $\delta$ is the ratio between the ABL and free tropospheric heights.

| Variable | Governing equation |
|---|---|
| $u_0$ | $\frac{D_0 u_0}{Dt} + \frac{\partial (u_1 v_1)}{\partial y} + \frac{\partial (u_2 v_2)}{\partial y} - \sqrt{2}\,(u_1 + u_2)\,\frac{\partial v_0}{\partial y} - y v_0 = \mathcal{S}_0^u$ |
| $v_0$ | $\frac{D_0 v_0}{Dt} + \frac{\partial (v_1 v_1)}{\partial y} + \frac{\partial (v_2 v_2)}{\partial y} - \sqrt{2}\,(v_1 + v_2)\,\frac{\partial v_0}{\partial y} + y u_0 = -\frac{\partial p_0}{\partial y} + \mathcal{S}_0^v$ |
| $u_1$ | $\frac{D_0 u_1}{Dt} + v_1 \frac{\partial u_0}{\partial y} + \frac{\sqrt{2}}{2}\left(v_1 \frac{\partial u_2}{\partial y} + v_2 \frac{\partial u_1}{\partial y} + 2 u_2 \frac{\partial v_1}{\partial y} + \frac{1}{2} u_1 \frac{\partial v_2}{\partial y}\right) - \left(\frac{1}{2} u_1 + \frac{8}{3} u_2\right) \frac{\partial v_0}{\partial y} - y v_1 = \mathcal{S}_1^u$ |
| $v_1$ | $\frac{D_0 v_1}{Dt} + v_1 \frac{\partial v_0}{\partial y} + \frac{\sqrt{2}}{2}\left(v_1 \frac{\partial v_2}{\partial y} + v_2 \frac{\partial v_1}{\partial y} + 2 v_2 \frac{\partial v_1}{\partial y} + \frac{1}{2} v_1 \frac{\partial v_2}{\partial y}\right) - \left(\frac{1}{2} v_1 + \frac{8}{3} v_2\right) \frac{\partial v_0}{\partial y} + y u_1 = \frac{\partial \theta_1}{\partial y} + \mathcal{S}_1^v$ |
| $\theta_1$ | $\frac{D_0 \theta_1}{Dt} - \frac{\partial v_1}{\partial y} + \frac{\sqrt{2}}{2}\left(2 v_1 \frac{\partial \theta_2}{\partial y} - v_2 \frac{\partial \theta_1}{\partial y} + 4 \theta_2 \frac{\partial v_1}{\partial y} - \frac{1}{2} \theta_1 \frac{\partial v_2}{\partial y}\right) + \left(\frac{1}{2} \theta_1 - \frac{8}{3} \theta_2\right) \frac{\partial v_0}{\partial y} + \sqrt{2} \frac{\partial v_0}{\partial y} = H_d - Q_{R,1} - \frac{1}{\tau_D} \theta_1$ |
| $u_2$ | $\frac{D_0 u_2}{Dt} + v_2 \frac{\partial u_0}{\partial y} + \frac{\sqrt{2}}{2}\left(v_1 \frac{\partial u_1}{\partial y} - u_1 \frac{\partial v_1}{\partial y}\right) + \left(\frac{2}{3} u_1 - \frac{1}{2} u_2\right) \frac{\partial v_0}{\partial y} - y v_2 = \mathcal{S}_2^u$ |
| $v_2$ | $\frac{D_0 v_2}{Dt} + v_2 \frac{\partial v_0}{\partial y} + \left(\frac{2}{3} v_1 - \frac{1}{2} v_2\right) \frac{\partial v_0}{\partial y} + y u_2 = \frac{\partial \theta_2}{\partial y} + \mathcal{S}_2^v$ |
| $\theta_2$ | $\frac{D_0 \theta_2}{Dt} + \frac{\sqrt{2}}{4}\left(v_1 \frac{\partial \theta_1}{\partial y} - \theta_1 \frac{\partial v_1}{\partial y}\right) - \frac{1}{4} \frac{\partial v_2}{\partial y} + \frac{1}{2}\left(\frac{4}{3} \theta_1 + \theta_2\right) \frac{\partial v_0}{\partial y} + \frac{\sqrt{2}}{4} \frac{\partial v_0}{\partial y} = \frac{1}{2}\left[H_c - H_s - Q_{R,2} - \frac{1}{\tau_D} \theta_2\right]$ |
| $q$ | $\frac{D_0 q}{Dt} + \frac{\partial}{\partial y}\left(\left(\tilde{\alpha}_1 v_1 + \tilde{\alpha}_2 v_2\right) q + \tilde{Q}_1 v_1 + \tilde{Q}_2 v_2 - \tilde{Q}_0 v_0\right) - \kappa q \frac{\partial v_0}{\partial y} = -\mathcal{P} + \mathcal{S}^q$ |
| $\theta_{eb}$ | $\frac{D_b \theta_{eb}}{Dt} = -E \Delta_t \theta_e - M_d \Delta_m \theta_e + \frac{1}{\tau_e} \Delta_s \theta_e - Q_{Rb}$ |
| $\theta_b$ | $\frac{D_b \theta_b}{Dt} = -E \Delta_t \theta - M_d \Delta_m \theta + \frac{1}{\tau_e} \Delta_s \theta - Q_{Rb}$ |
| $u_b$ | $\frac{D_b u_b}{Dt} - y v_b = -E_u \Delta_t u - C_d U u_b$ |
| $v_b$ | $\frac{D_b v_b}{Dt} + y u_b = -\frac{\partial p_b}{\partial y} - E_u \Delta_t v - C_d U v_b$ |
| | Continuity of vertical velocity: $\frac{\partial v_0}{y} = \delta \frac{\partial v_b}{y}$ |
| | Continuity of total pressure: $p_0 = p_b + \delta \frac{\pi}{2} \theta_b + \sqrt{2}(\theta_1 + \theta_2)$ |

TABLE 2. Multicloud model and ABL model with closure equations for all forcing terms appearing in the governing equations in Table.1. The primes stand for deviations from the radiative convective equilibrium (RCE) solution. The expression with the superscript + has the same value as that inside the bracket if the latter has positive value and vanish if its value is negative or zero.

| Forcing term | Closure equation |
|---|---|
| Momentum turbulent drag for barotropic mode | $\mathcal{S}_0^{\boldsymbol{u}} = \delta E_{\boldsymbol{u}} \Delta_t \boldsymbol{u}$ |
| Momentum turbulent drag for baroclinic modes | $\mathcal{S}_j^{\boldsymbol{u}} = \frac{\sqrt{2}\delta}{\tau_T}\Delta_t \boldsymbol{u} - \frac{1}{\tau_R}\boldsymbol{u}_j, j = 1,2$ |
| Velocity jump at top of ABL | $\Delta_t \boldsymbol{u} = \boldsymbol{u}_b - \boldsymbol{u}_0 - \sqrt{2}\left(\boldsymbol{u}_1 + \boldsymbol{u}_2\right)$ |
| Congestus heating | $\frac{\partial H_c}{\partial t} = \frac{1}{\tau_c}\left(\alpha_c \Lambda Q_c - H_c\right)$ |
| Deep convective heating | $H_d = \left(1-\Lambda\right) Q_d$ |
| Stratiform heating | $\frac{\partial H_s}{\partial t} = \frac{1}{\tau_s}\left(\alpha_s H_d - H_s\right)$ |
| Bulk energy available for congestus convection | $Q_c = \left\{\bar{Q} + \frac{1}{\tau_{conv}}\left[\theta'_{eb} - a'_0\left(\theta'_1 + \gamma'_2\theta'_2\right)\right]\right\}^+$ |
| Bulk energy available for deep convection | $Q_d = \left\{\bar{Q} + \frac{1}{\tau_{conv}}\left[a_1\theta'_{eb} + a_2 q' - a_0\left(\theta'_1 + \gamma_2\theta'_2\right)\right]\right\}^+$ |
| Moisture switch function | $\Lambda = \begin{cases} 1, & for \quad \Delta_m\theta_e \geq \theta^+ \\ 0, & for \quad \Delta_m\theta_e \leq \theta^- \\ linear\ and\ continuous, & for \quad \theta^- < \Delta_m\theta_e < \theta^+ \end{cases}$ |

Table 2 (continued).

| | |
|---|---|
| Precipitation rate | $\mathcal{P} = \frac{2\sqrt{2}}{\pi} H_d$ |
| Moisture source | $\mathcal{S}^q = \delta E \Delta_t \theta_e + \left(\delta M_d + \frac{\partial v_0}{\partial y}\right) \Delta_m \theta_e$ |
| Equivalent potential temperature at top of ABL | $\theta_{et} = \kappa q$ |
| Equivalent potential temperature at the middle troposphere | $\theta_{em} = q + \frac{2\sqrt{2}}{\pi} (\theta_1 + \alpha_2 \theta_2)$ |
| Total downdraft mass flux | $M_d = \{D_c + \frac{\partial v_b}{\partial y}\}^+$ |
| Convective updraft mass flux | $M_u = \frac{1}{\alpha_m} D_c$ |
| Mass flux velocity from large-scale and convective downdrafts | $D_c = m_0 \{1 + \frac{\mu}{\bar{Q}} (H_s - H_c)\}^+$ |
| Moist thermodynamic turbulent entrainment velocity at top of ABL | $E = \left(M_u - M_d + \frac{\partial v_b}{\partial y}\right)^+$ |
| Momentum turbulent entrainment velocity at top of ABL | $E_u = \left(\frac{1}{\tau_T} + \frac{\partial v_b}{\partial y}\right)^+$ |

TABLE 3. Constant and parameters in the multicloud model and ABL model.

| Parameter | Value | Description |
|---|---|---|
| $H_T$ | 16 km | height of the free troposphere |
| $h_b$ | 500 m | ABL depth |
| $\delta$ | 0.03125 | Ratio of ABL depth to height of the troposphere |
| $\kappa$ | 1.25 | Ratio of moisture at top of ABL to that in the free troposphere |
| $\bar{Q}$ | 1.11 K day $^{-1}$ | Heating potential at RCE |
| $Q_{R1}$ | 1 K day$^{-1}$ | Longwave first baroclinic radiative cooling rate |
| $Q_{R2}$ | -0.226 K day$^{-1}$ | Longwave second baroclinic radiative cooling rate |
| $Q_{Rb}$ | 5.11 K day$^{-1}$ | ABL radiative cooling rate |
| $m_0$ | $5.12 \times 10^{-3}$ m s$^{-1}$ | Downdraft velocity reference scale |
| $\alpha_c, \alpha_s$ | 0.22, 0.25 | Congestus, stratiform adjustment coefficient |
| $a_0$ | 3 | Contribution of $\theta_1$ to deep convective heating anomalies |
| $a_1$ | 0.45 | Contribution of $\theta_{eb}$ to deep convective heating anomalies |
| $a_2$ | 0.55 | Contribution of $q$ to deep convective heating anomalies |
| $\gamma_2$ | 0.1 | Relative contribution of $\theta_2$ to deep convective heating anomalies |
| $a_0'$ | 1.7 | Contribution of $\theta_1$ to shallow heating anomalies |
| $\gamma_2'$ | 2 | Relative contribution of $\theta_2$ to shallow heating anomalies |
| $\alpha_2$ | 0.1 | Relative contribution of $\theta_2$ to $\theta_{em}$ |
| $\mu$ | 0.25 | Contribution of convective downdrafts to $M_d$ |
| $\tau_c, \tau_s$ | 1 h, 3 h | Congestus, stratiform adjustment timescales |
| $\tau_{conv}$ | 2h | Convective timescale |
| $\theta^-, \theta^+$ | 10 K, 20 K | Moisture switch threshold values |

Table 1 (continued).

| Parameter | Value | Description |
|---|---|---|
| $\tau_D$ | 50 days | Newtonian cooling timescale |
| $\tau_R$ | 75days | Rayleigh drag timescale |
| $\tau_T$ | 8h | Momentum entrainment timescale |
| $\tau_e$ | 7.08 h | Surface evaporation timescale |
| $U$ | $2m/s$ | Strength of turbulent velocity |
| $C_d$ | 0.001 | Surface drag coefficient |
| $\alpha_m$ | 0.2 | Ratio of $D_c$ to $M_u$ |
| $\tilde{\alpha}_1$ | 1 | First baroclinic coefficient of nonlinear moisture flux anomaly |
| $\tilde{\alpha}_2$ | .1 | Second baroclinic coefficient of nonlinear moisture flux anomaly |
| $\tilde{Q}_0$ | 1.674 (non dim.) | Bartopic mode coefficient of background moisture convergence |
| $\tilde{Q}_1$ | 0.558 (non dim.) | First baroclinic coefficient of background moisture convergence |
| $\tilde{Q}_2$ | 0.212 (non dim.) | Second baroclinic coefficient of background moisture convergence |

# LIST OF FIGURES

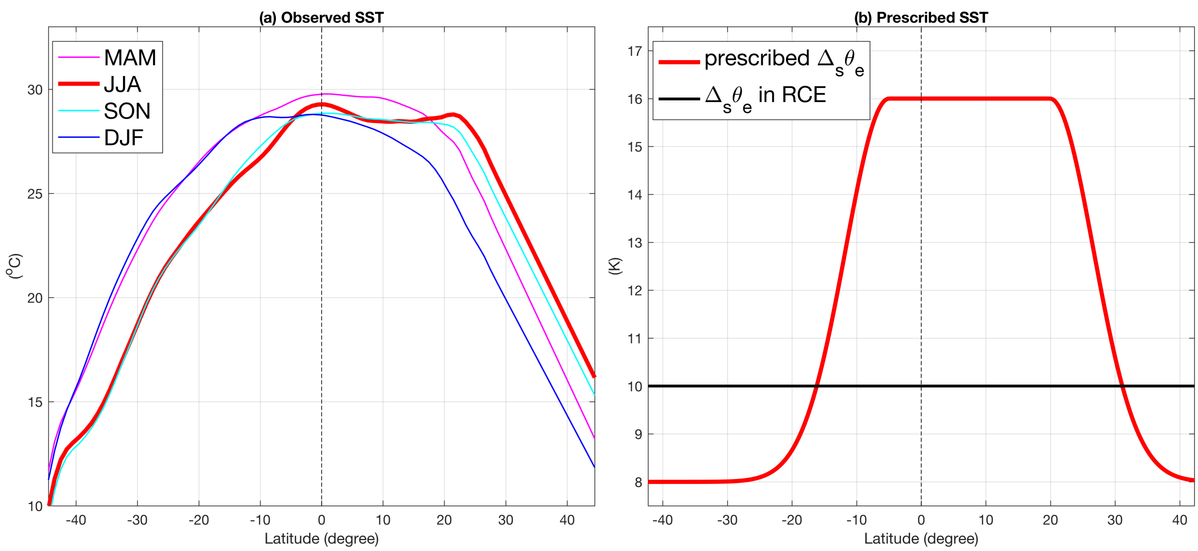


FIG. 1. Meridional profiles of SST over the Indian Ocean monsoon region. Panel (a) shows climatological mean of seasonal mean of observed SST (° C) averaged over the period (July 1981 – June 2016) and the longitude range 60° E – 90° E, based on NOAA Optimum Interpolation SST V2 data product. The four curves in different colors correspond to different seasons. Panel (b) shows the prescribed $\Delta_s\theta_e$ ($K$) in a red curve and its mean value in a black line. The dashed lines in both panels show the equator.

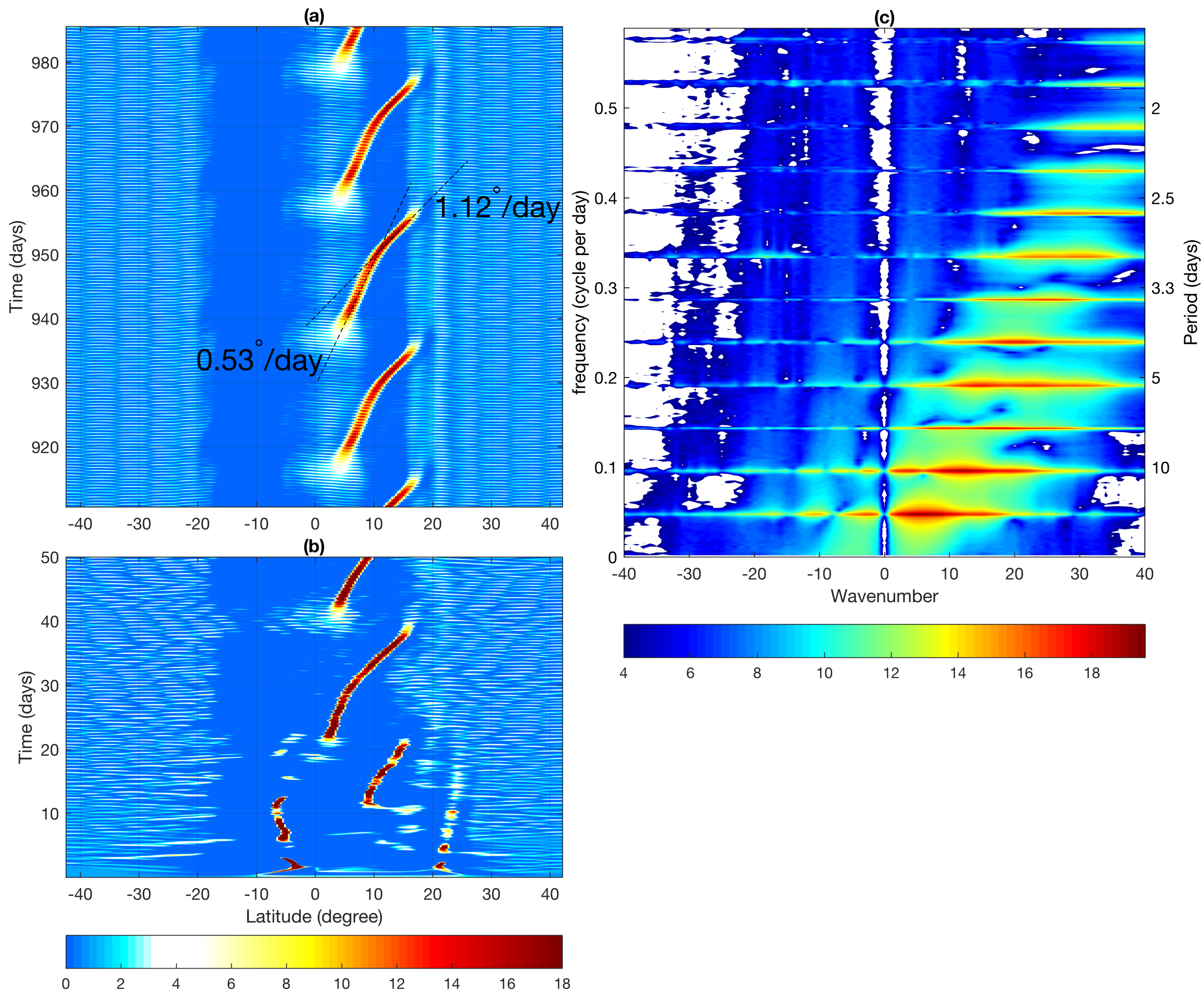


911 FIG. 2. Northward propagation of precipitation. Panel (a) and (b) show the Hovmöller diagram of precipitation during the statistical equilibrium period (Days 910 to 985) and the first 50 day transient period, respectively. The dashed lines indicate the propagation speeds of the northward-moving precipitation as it transitions between the low latitude and high latitude regimes. Panel (c) shows the spectral diagram for precipitation variability between Day 509 and Day 1019. The dimensional unit of precipitation is K day$^{-1}$.

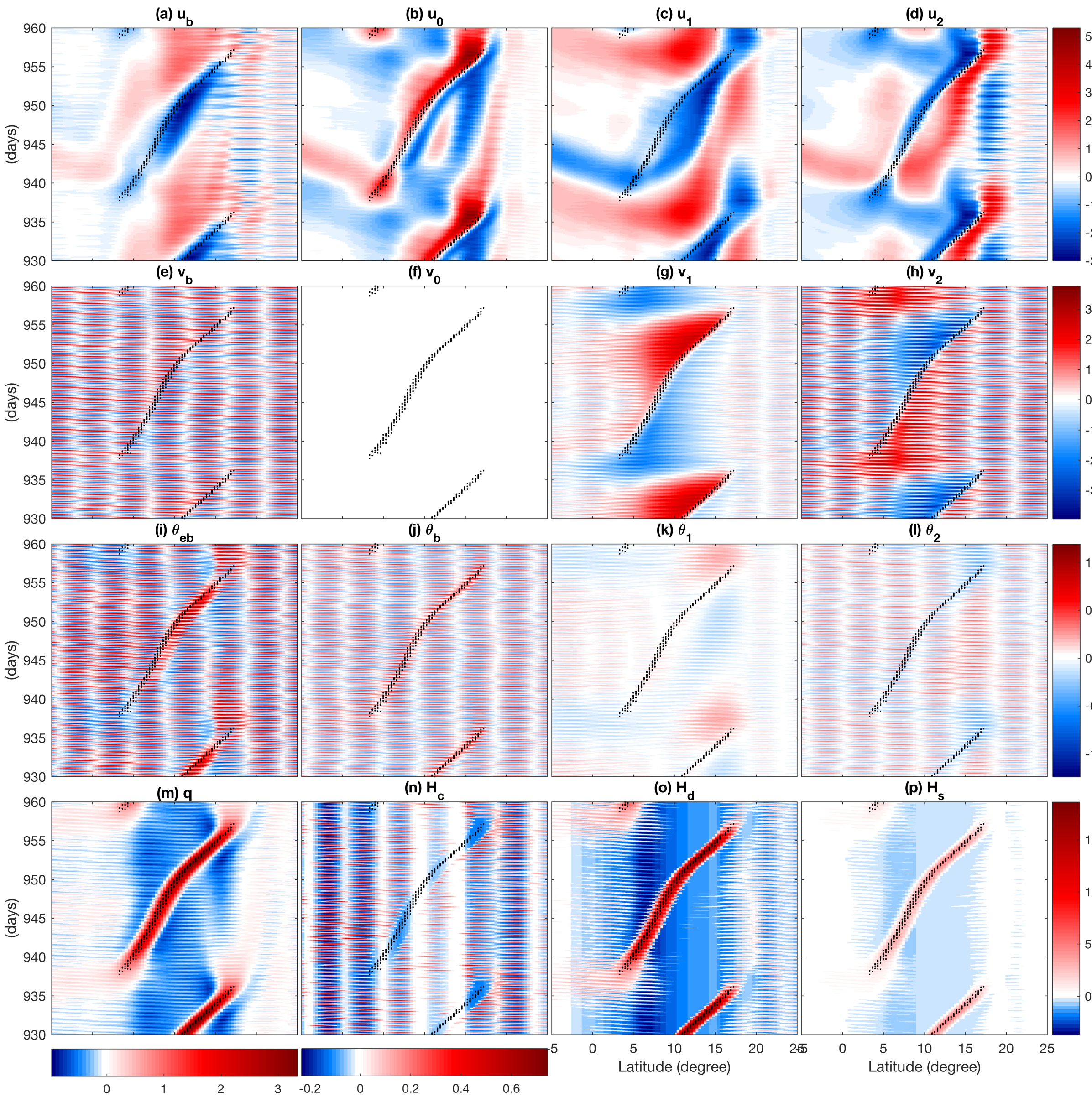


FIG. 3. Hovmöller diagrams for all flow field anomalies (deviation from the climatological mean). In the first three rows (a-l), the panels from top to bottom are for zonal velocity ($ms^{-1}$), meridional velocity ($ms^{-1}$) and potential temperature (K), while those from left to right are for the ABL, barotropic, first- and second-baroclinic modes. The last row of panels from left to right show moisture (K), congestus, deep and stratiform heating ($Kday^{-1}$). East row of panels share the same colorbar at the right hand side, except for panels (m,n) with their own colorbar at the bottom. The black dots show the latitude of the maximum precipitation anomalies at each time step.

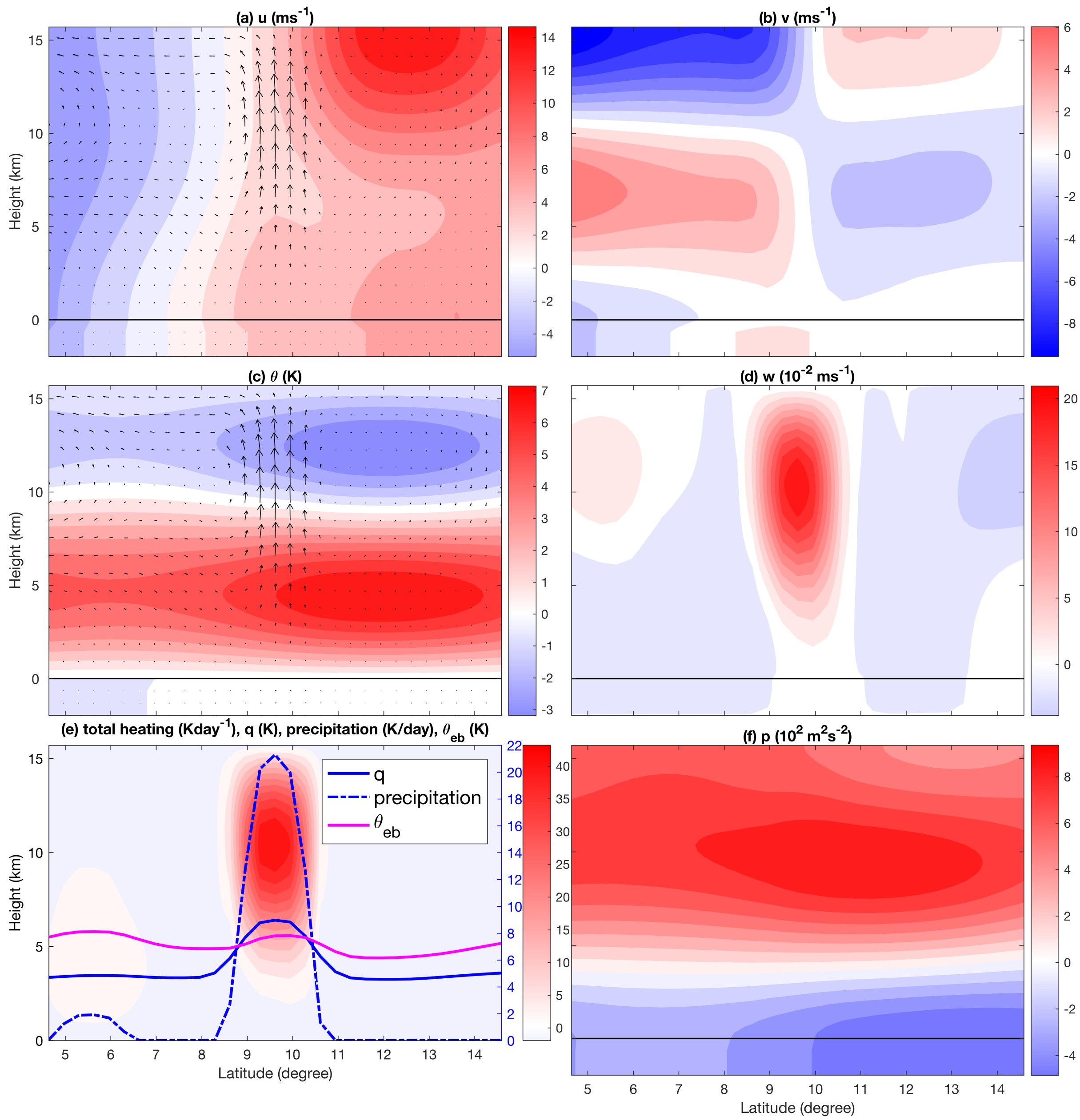


923 FIG. 4. Meridional circulation at the early stage of the simulation (Day 33.3) in the latitude-height diagram. These panels show (a) zonal velocity, (b) meridional velocity, (c) potential temperature, (d) vertical velocity, (e) total heating (color contours), (f) pressure. The arrows in panel (a) and (c) show meridional circulation $(v,w)$. In panel (e), dimensionless value of moisture (solid blue curve), boundary layer equivalent potential temperature (purple), and precipitation (dashed blue curve) are shown by the right axis. The bold black line indicates the interface between free troposphere and ABL. Their dimensional units are shown in the subtitles of each penal.

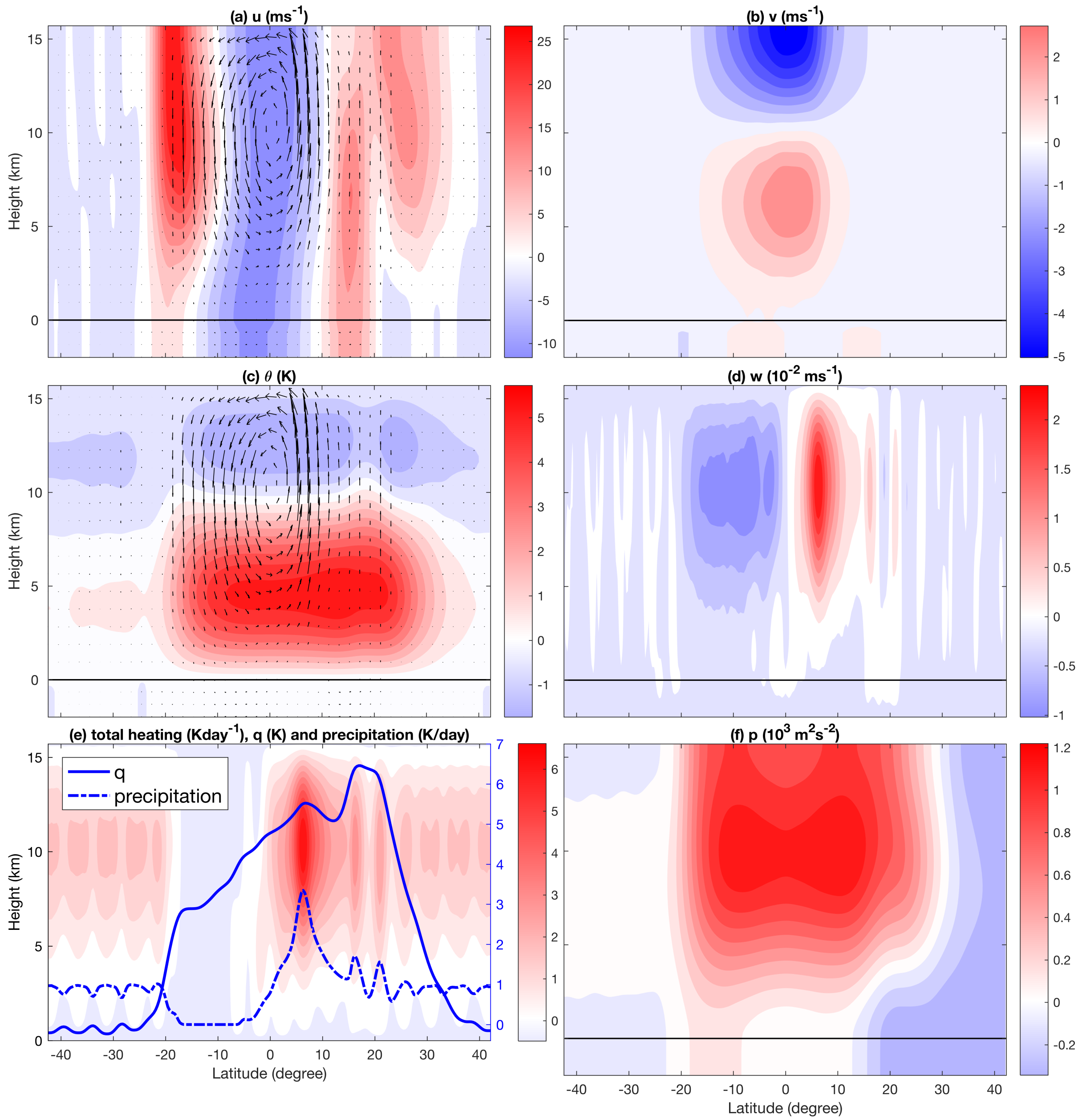


FIG. 5. Similar to Fig.3 but for climatological mean circulation averaged over the period (Day 509∼Day 1019)

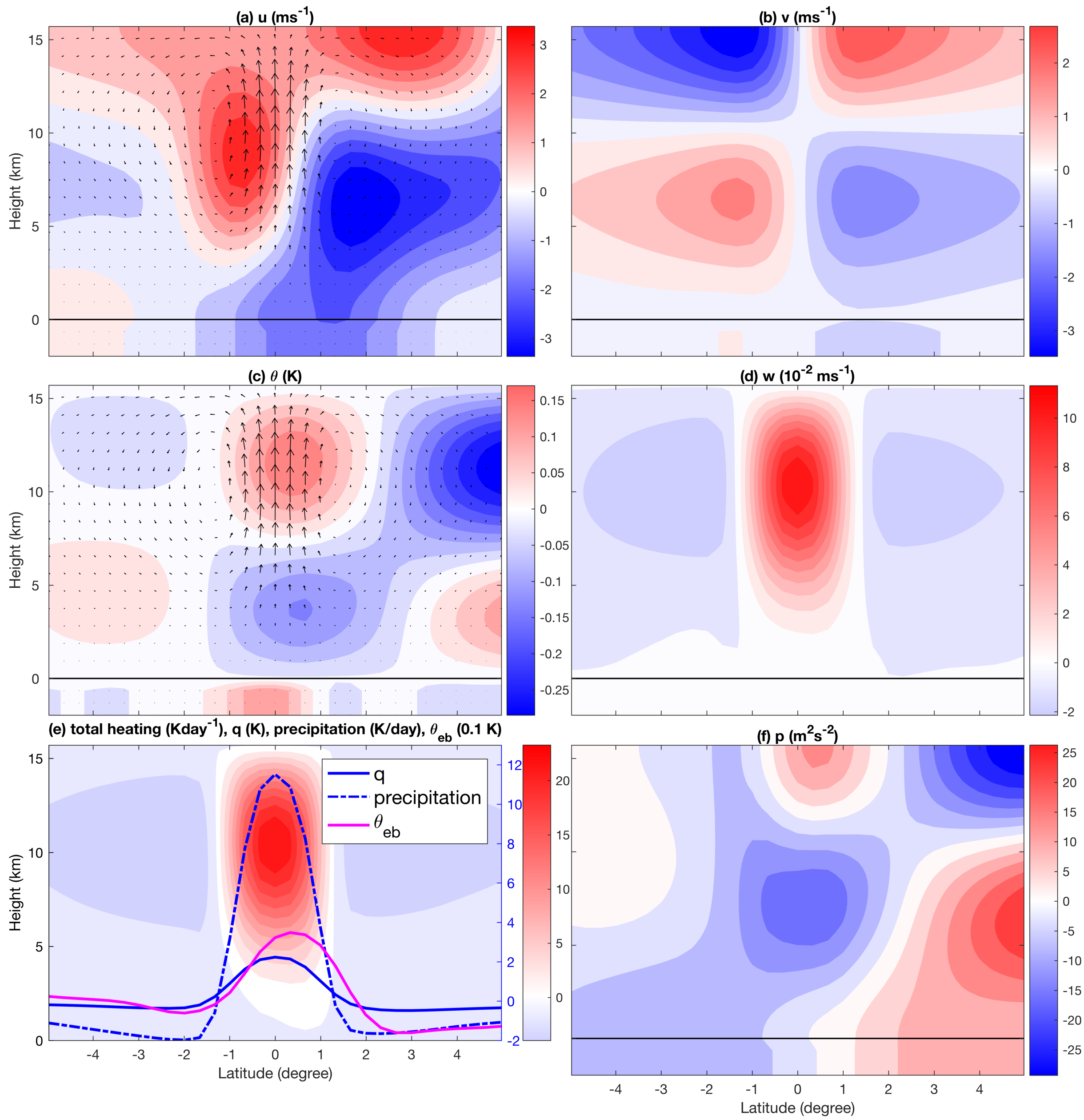


929 FIG. 6. Similar to Fig.3 but for vertical structure of composite flow field anomalies (deviation from the climatological mean) correlated with the northward-propagating precipitation between Day 935 and Day 955 in the latitude-height diagram. The center latitude (0 degree) corresponds to the latitude where the maximum precipitation is located.

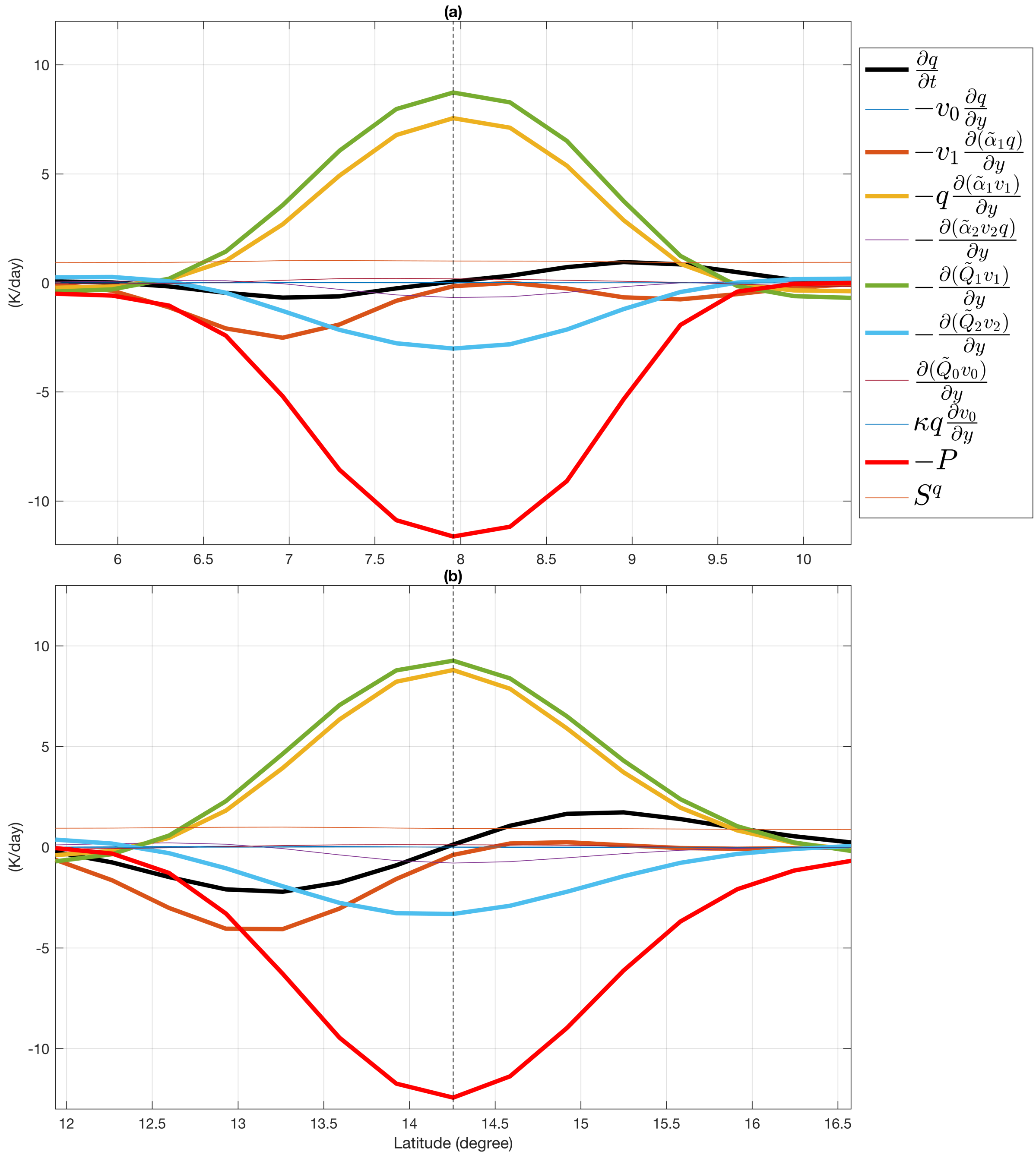


FIG. 7. Moisture budget analysis for all terms appearing in the free tropospheric moisture equation. Panel (a) is for the case when the maximum precipitation is located at $7.9°N$, and panel (b) is at $14.25°N$. The curves in different colors correspond to different terms as shown in the legend. Only the latitude range in the neighbor of the maximum precipitation is shown here. All dominant terms are shown in bold curves. The dashed lines indicate the latitude with the maximum precipitation.

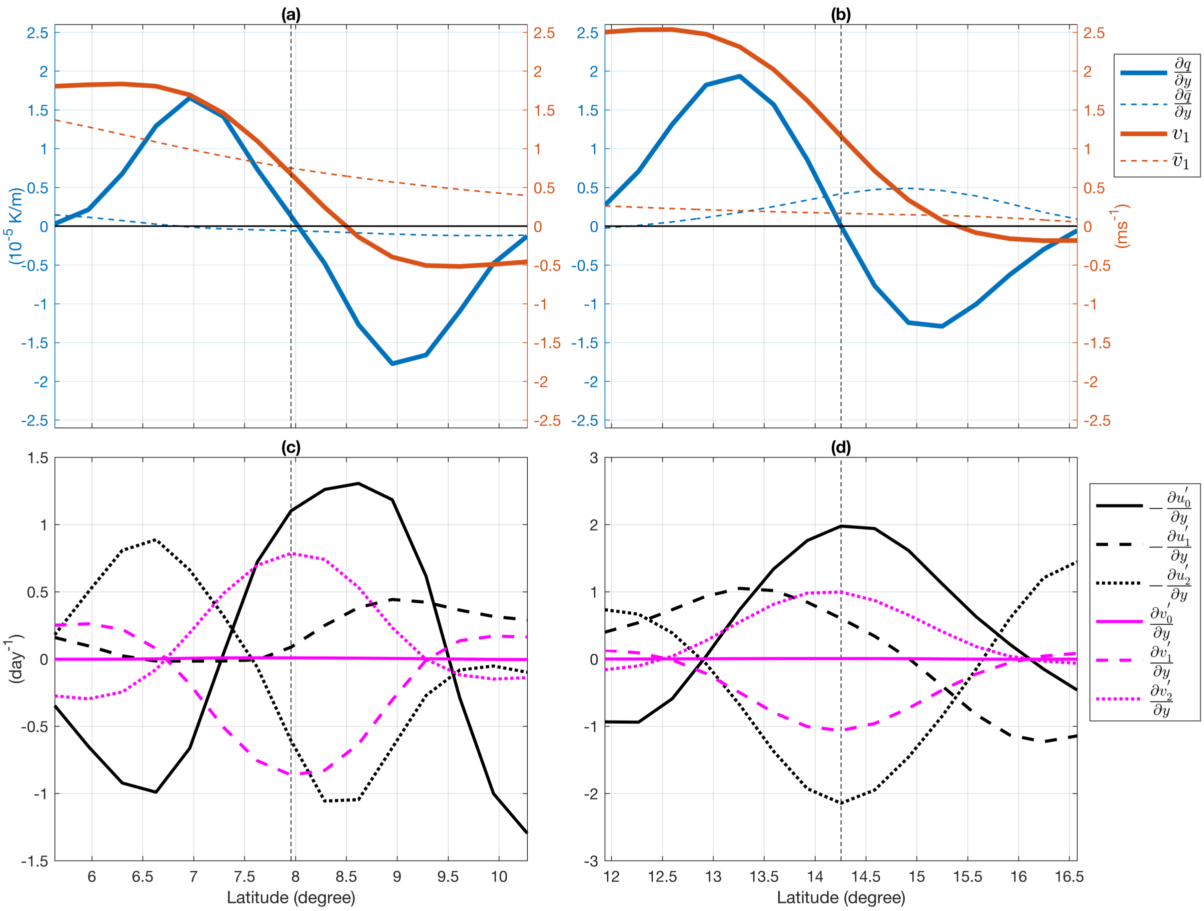


FIG. 8. Meridional profiles of moisture gradient, meridional velocity, vorticity and divergence. Panels (a,b) show moisture gradient in blue curves and first-baroclinic meridional velocity in red curves. The solid curves are for total value and the dashed curves are for climatological mean. The solid black line shows zero magnitude. Panels (c,d) show barotropic, first- and second-baroclinic vorticity anomalies in black curves and divergence anomalies in pink curves. The left panels (a,c) are for the case when the maximum precipitation is located at $7.9°N$, and panel (b,d) are at $14.25°N$.

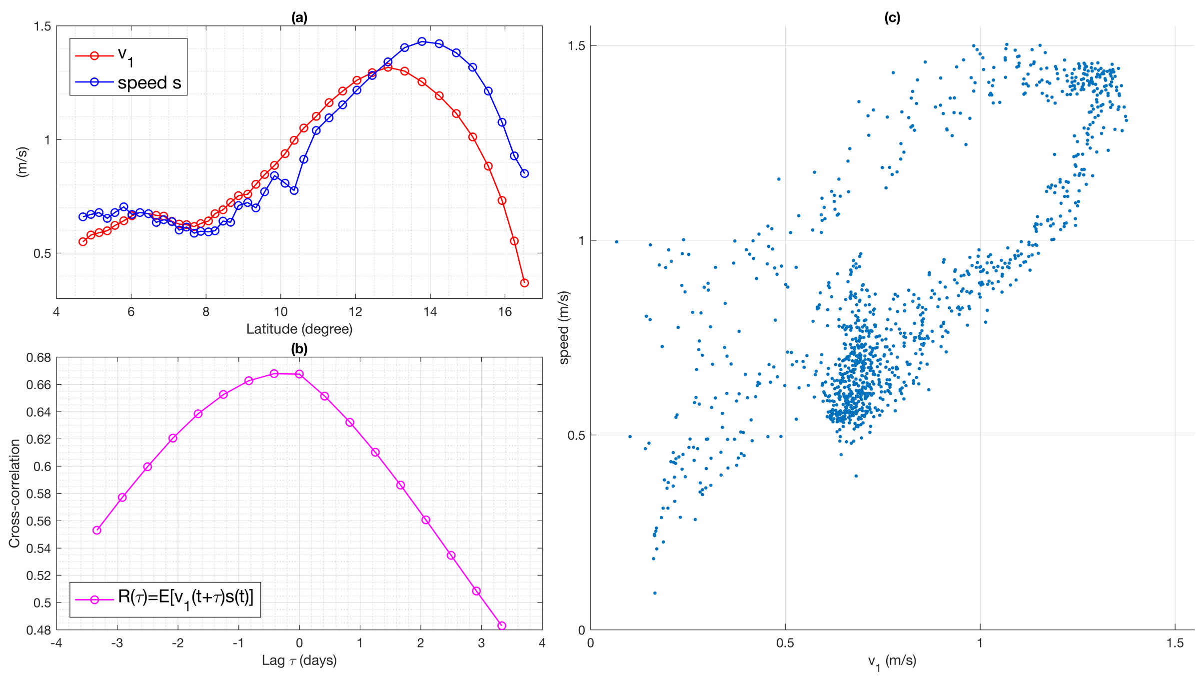


FIG. 9. The phase relation between local mean first-baroclinic meridional velocity $v_1$ and propagation speed $s$ of the maximum precipitation. Panel (a) shows their magnitude when the maximum precipitation reaches each latitude after equal time interval. Panel (b) shows cross correlation between $v_1$ and $s$. Panel (s) is the scatter plot for all sample snapshots during 24 northward propagating events. Here $v_1$ is averaged over 4.64° latitude range centered about the maximum precipitation.

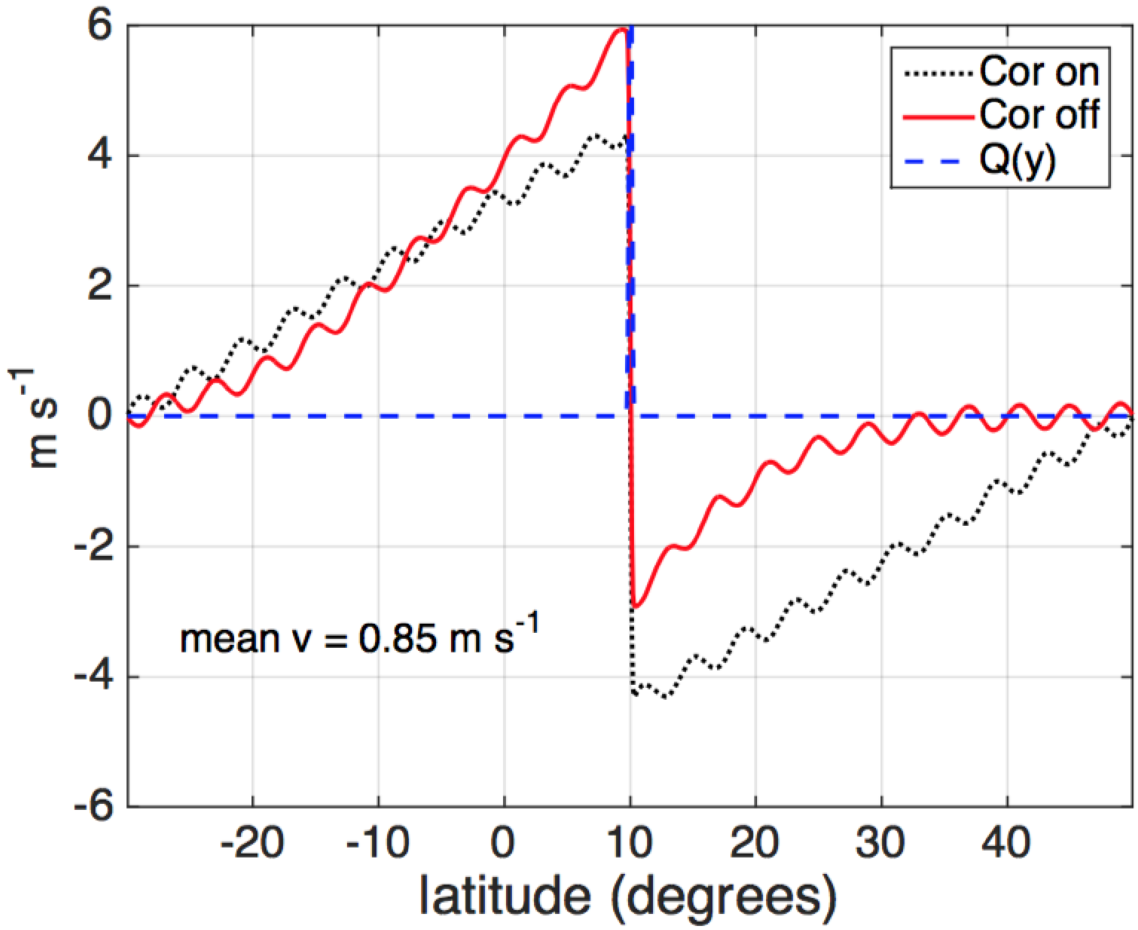


FIG. 10. Solution of the wave equation in (6) at 200 days both with (solid) and without (dots) the Coriolis gradient parameter. The dashed line in the background is the imposed heating profile.

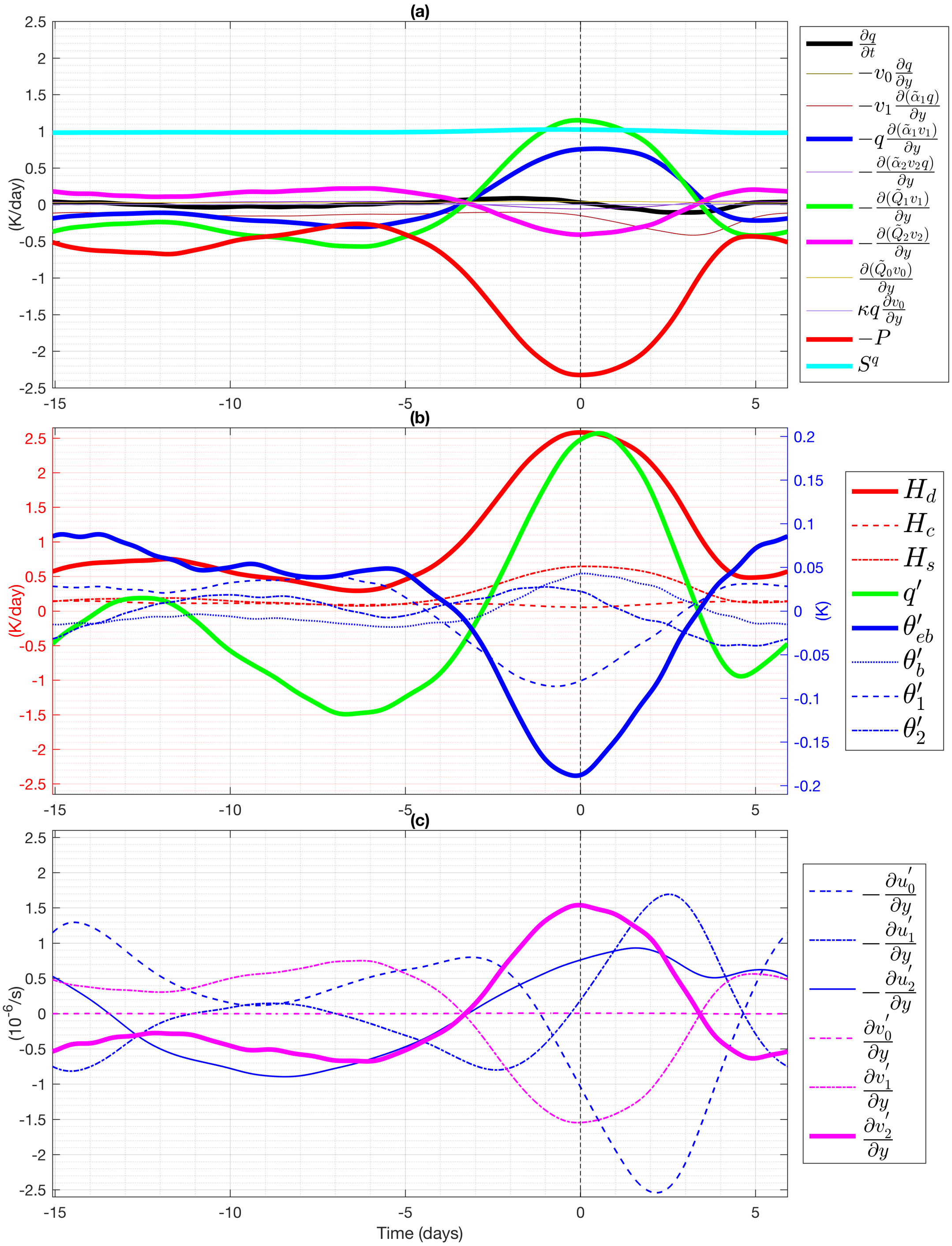


FIG. 11. Time series of moisture budget terms (a), heating rates and thermodynamic fields (b), and vorticity and divergence during the initiation of BSISO events near the equator. All variables have been averaged between 5° S and 5° N and the resulting time series have been processed by a low-pass filter and all signals with period less than 1 day are filtered out.

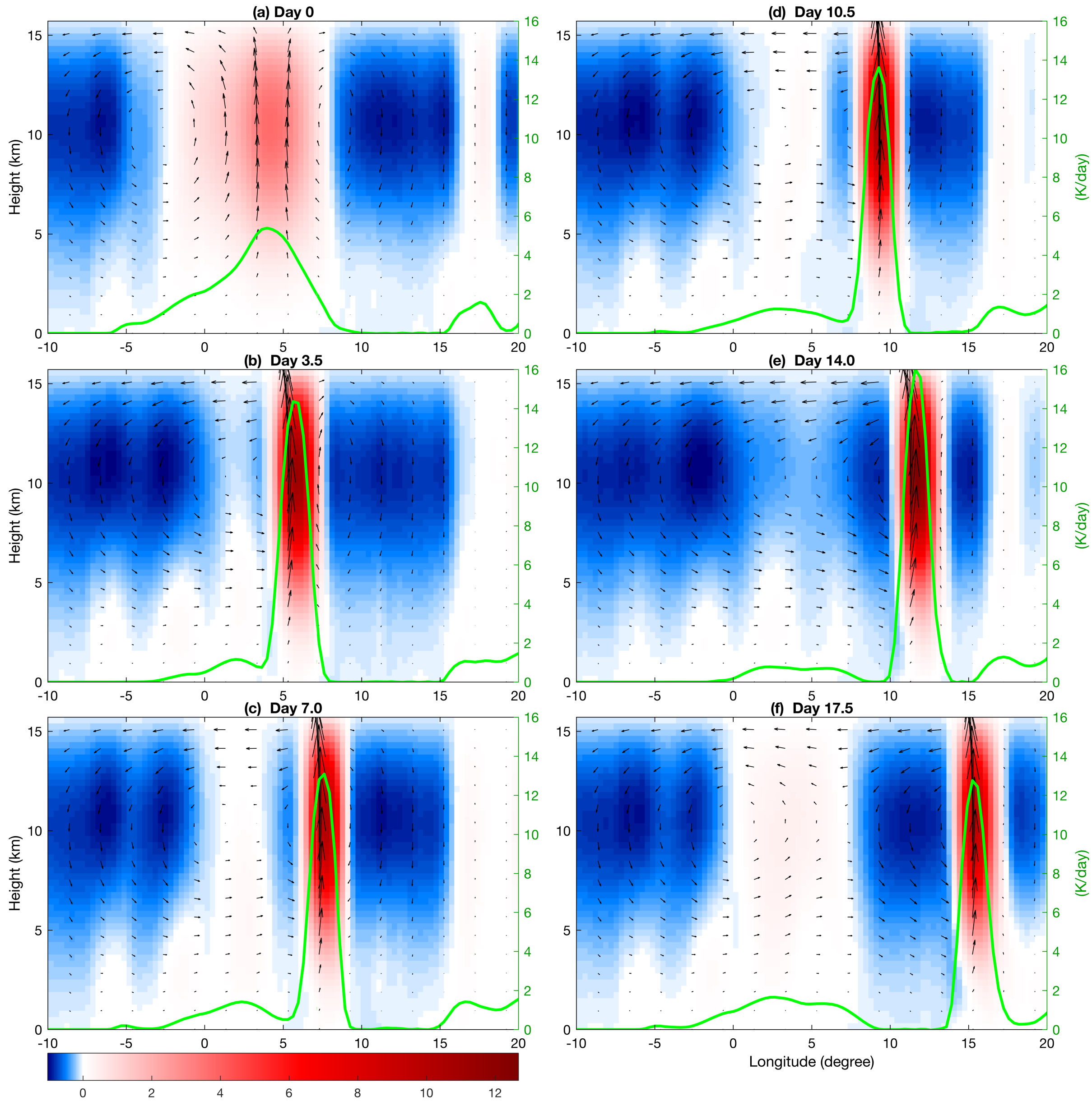


FIG. 12. Meridional circulation at six different phases in the latitude-height diagram. These six panels are from different phases of the composite life cycle of northward propagating events with 3.5 days time interval. Meridional and vertical velocity are shown by arrows and vertical velocity is also shown by color. The green curve in each panel shows meridional profile of deep heating with its magnitude indicated by the right axis. The dimensional units of vertical velcity and deep heating are $10^{-2} m/s$ and $K/day$.

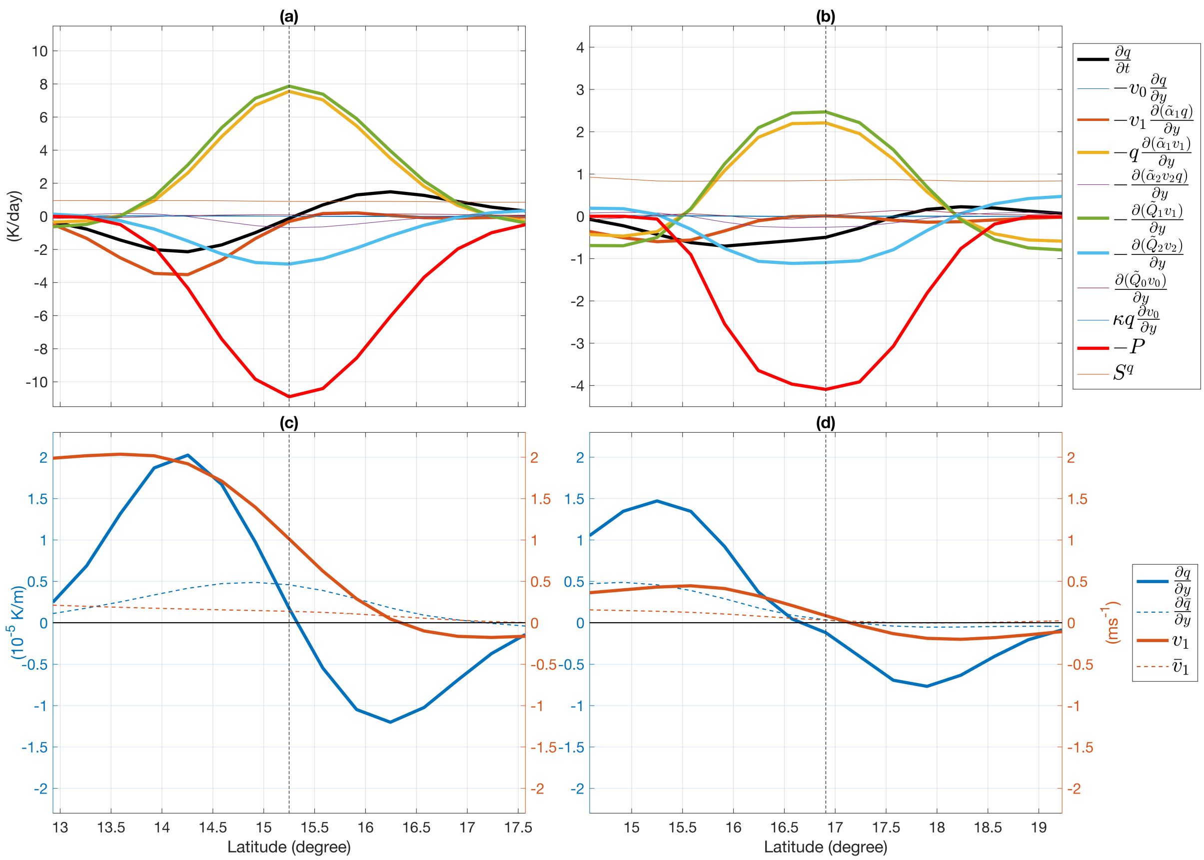


FIG. 13. Panels (a) and (b) are similar to Fig.7 but for cases when maximum precipitation is located at (a)15.25°$N$ and (b) 16.9°$N$ while Panels (c) and (d) are the respective equivalents of Panels (a)-(b) in Figure 8.